Universidade de Aveiro

Departamento de Física

2011

Luis Carlos Ávila Leal

Espectroscopia de absorção de intracavidade com lasers de fibra dopada com Er^{3+}

Intracavity absorption spectroscopy with Er^{3+}-doped fiber lasers

Universidade de Aveiro

Departamento de Física

2011

Luis Carlos Ávila Leal

Espectroscopia de absorção de intracavidade com lasers de fibra dopada com Er^{3+}

Intracavity absorption spectroscopy with Er^{3+}-doped fiber lasers

dissertação apresentada à Universidade de Aveiro para cumprimento dos requisitos necessários à obtenção do grau de Mestre em Engenharia Física, realizada sob a orientação científica do Prof. Dr. Mário Ferreira, Professor associado com agregado do Departamento de Física da Universidade de Aveiro

o júri

presidente	**Prof. Doutor João Filipe Calapez de Albuquerque Veloso** Professor Auxiliar do Departamento de Física da Universidade de Aveiro
arguente	**Prof. Doutor Paulo Vicente da Silva Marques** Professor Auxiliar do Departamento de Física e Astronimia da Faculdade de Ciências da Universidade do Porto
orientador	**Prof. Doutor Mário Fernando dos Santos Ferreira** Professor Associado com agregação do Departamento de Física da Universidade de Aveiro

agradecimentos

O trabalho realizado nesta tese contou com a contribuição de algumas pessoas. Em primeiro lugar ao meu orientador Professor Valeri Baev da Universidade de Hamburgo pela oportunidade de me juntar ao seu grupo de investigação, e claro pelo seu apoio prestado ao longo do desenvolvimento do meu trabalho.
Ao Professor Mário Ferreira pelo seu apoio e dedicação para que fosse possível a minha colocação no grupo do Professor Baev, sobre a sua própria orientação.
Aos meus colegas Peter Fjodorow e Benjamin Löhden por me terem guiado num bom sentido à realização do trabalho e me terem facilitado a integração no grupo.
Ao Ortwin Hellmig pela ajuda na preparação das fibras.
Aos meus pais pelo seu apoio pessoal e financeiro.
À Universidade de Aveiro e Universidade de Hamburgo pelas condições fornecidas para a realização deste trabalho.

palavras-chave

lasers de fibra, fibra dopada com Er^{3+}, espectroscopia de absorção de intracavidade, medidas de absorção, sensibilidade, concentração de CO_2

resumo

Espectroscopia de absorção de intracavidade com um laser de banda larga de fibra dopada com Er^{3+} é aplicada para medidas resolvidas no tempo de moléculas de CO_2 revelando informações quantitativas sobre a concentração do gás exalado na respiração humana. A gama espectral das medições estende-se de 1.52 µm – 1.61 µm através da deslocação da lente de intracavidade. Com um laser pulsado aplicado nesta experiência, a sensibilidade à absorção corresponde a um comprimento do percurso de absorção efectiva de 6 km assumindo que a cavidade está completamente preenchida com a amostra. O aumento da sensibilidade é alcançada através da construção de um laser de configuração em anel unidirecional. O comprimento do percurso de absorção efectiva é aumentado por um factor de três comparando com uma configuração linear com o mesmo comprimento da cavidade.

keywords

fiber lasers, Er^{3+}-doped fiber, intracavity absorption spectroscopy, absorption measurements, sensitivity, CO_2 concentration

abstract

Intracavity absorption spectroscopy with a broadband Er^{3+}-doped fiber laser is applied for time-resolved measurements of CO_2 molecules revealing quantitative information about the gas concentration in exhaled human breath.
The spectral range of measurements extends from 1.52 to 1.61 µm by moving an intracavity lens. With a pulsed laser applied in this experiment, the sensitivity to absorption corresponds to an effective absorption path length of 6 km assuming the cavity is completely filled with the sample. Sensitivity enhancement is achieved by employing an unidirectional ring laser. The effective absorption path length is enhanced by a factor of three compared to a linear configuration with the same cavity length.

Table of Contents

Table of Figures

Introduction

Since the development of optical spectroscopy, spectroscopic techniques have been continuously developed and now offer a wide range of applications. The elaboration of novel methods is therefore of fundamental importance both for scientific research and for manufacturing industry. Absorption spectroscopy is commonly used for various diagnostic purposes, such as for environmental, combustion analysis, plasma research, medicine and determination of stable isotope ratios. Wavelength and intensity of light absorbed provide information about the composition of samples and about the inner structure of atoms and molecules involved, such as the location and the occupation of their energy states.

For many applications it is necessary a simultaneous detection of several molecules in small concentrations in a dynamic environment. For this purpose, methods are needed having high sensitivity, high time resolution, high stability to broadband losses and allow the simultaneous detection of several molecules. The detection limit of absorption measurements is determined by the absorption path length and by the signal-to-noise ratio. Highly sensitive methods are therefore characterized by either long absorption path lengths or by a particularly low noise level.

Many spectroscopy techniques use narrowband light sources, which have to be tuned, and are therefore not suitable in environments with turbulence or with non-stationary processes. Only with absorption spectroscopy in the laser resonator all the above requirements can be fulfilled.

Each broadband multimode laser, whose homogeneous linewidth is larger than the absorption linewidth of the sample, can be used for intracavity absorption spectroscopy.

Fiber lasers offer a particularly compact construction, high efficiency, broad emission bandwidth and tunability over a large spectral range. Er^{3+}-doped fiber lasers are suitable for the development of versatile ultra-sensitive gas detectors, since its tuning range extends from 1.52 µm to 1.62 µm and includes strong absorption of many molecules such as CO, CO_2, OH, HCN, C_2H_2, H_2S, NH_3, CH_4 and HI and only a few absorption lines occur from water vapor. In the present work, a compact and efficient gas analysis system consisting of Er^{3+}-doped fiber lasers is developed. This system allows absorption measurements of multiple gases simultaneously in real time.

The aim of this work involves an accurate online determination of gas concentrations present in human exhaled breath. The development of a compact and inexpensive system for the determination of molecular concentrations has a great importance for medical diagnostics. A prominent example of breath testing based on CO_2 is the non-invasive verification of *Helicobacter pylori* infection in the gastrointestinal tract by means of a $^{13}CO_2$ / $^{12}CO_2$ isotope ratio breath test. Nowadays, the evaluation of the breath test takes place with large mass spectrometers, which are expensive to purchase and to operate. Moreover it takes a long time to obtain the outcome. With the development of a diagnostic device based on compact fiber lasers would create many benefits for the field of breath analysis.

1 Fiber Lasers

Lasers comprise an optical resonator, which allows the light to circulate between two reflective components (mirrors), an active medium for light amplification, and a pump source that injects the light or electric current into the active medium. In order to convert an optical fiber into a fiber laser, it is required to place the fiber doped with active ions inside a cavity designed to provide optical feedback [1].

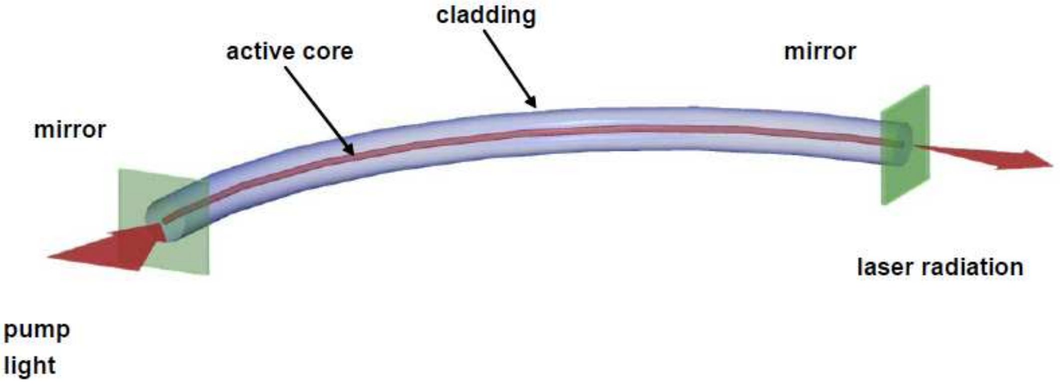

Figure 1.1 Schematic illustration of a fiber laser.

Fig. 1.1 shows a fiber laser on its simplest form. In general, both the pump and laser radiation are guided in an active doped waveguide structure, e.g. fiber. The laser cavity can be constructed by dielectric mirrors or fiber Bragg gratings on the fiber edges. This complete integration of the laser process leads to the inherent compactness and long-term stability of fiber lasers, because no free-space cavity is necessary [2].

1.1 Basic Concepts

A fiber laser is a solid-state laser whose active medium is the core of an optical fiber doped with rare earth elements, such as neodymium, thulium, ytterbium or erbium. Nevertheless there are also non-doped fibers lasers such as Brillouim and Raman fiber lasers. They exploit respectively Brillouim scattering and Raman scattering effect at the shifted stokes wavelength [3]. Doped-fiber lasers will be however mainly discussed in more detail due to their relevance for absorption measurements. Its basic structure comprises the doped core positioned between two mirrors adjacent to its end faces, which form the laser cavity. Fiber lasers allows an operation over a wide wavelength range from 0,4 µm to 4 µm [4]. The light from the pumping laser source (usually semiconductors laser diodes) is launched through one mirror into the fiber core which is waveguiding resonant structure forming a Fabry-Pérot cavity. The optical output is coupled through the mirror on the other end of the fiber. Therefore the fiber laser is effectively an optical wavelength converter in which the photons at the pumping wavelength are absorbed to produce the required population inversion and stimulated emission, thus providing a lasing output at a wavelength which is characterized by the dopant within the fiber core. Fiber lasers have very long gain regions and therefore a long interaction length of pump and laser field. Moreover, fiber lasers can generate very high output powers because the fiber’s high surface area to volume ratio prevents excessive heating and thus results in very high efficiencies. They can as well generate lower powers with very high beam quality, spectral purity and stability [1][4][5].

1.2 Light Propagation along an Optical Fiber

The structure of an optical fiber consists in a core with a refractive index n_1 surrounded by a cladding of slightly lower refractive index n_2. The cladding supports the waveguide structures and when sufficient thick, reduces the radiation loss into the surrounding air. The light energy travels in both the core and cladding allowing the associated fields to decay to a negligible value at the cladding-air interface. When a ray is incident on the interface between two dielectrics of different refractive indices (e.g. glass-air), refraction occurs. The ray approaching the interface is propagating in a dielectric of refractive index n_1 and is at an angle θ_1 to the normal at the surface of the interface. If the dielectric on the other side of the interface has a refractive index n_2 which is less than n_1, then the refraction is such that the ray path in this lower index medium is at an angle θ_2 to the normal, where θ_2 is greater than θ_1.

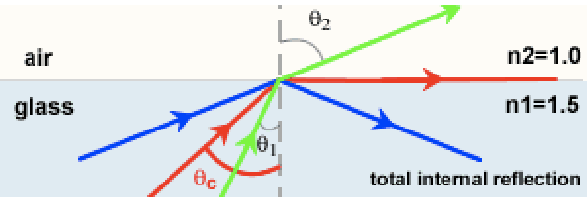

Figure 1.2 Light rays incident in a high to low refractive index interface.

The angles of incident and refraction are related to each other and to the refractive indices of the dielectrics according to Snell’s law of refraction, which states

$$n_1 \sin\theta_1 = n_2 \sin\theta_2 \tag{1.1}$$

a small amount of light is reflected back into the original dielectric medium (partial internal reflection). As n_1 is greater than n_2, the angle of refraction is 90° and the diffracted ray emerges parallel to the interface between the dielectrics, the angle of incidence must be less than 90°. This is the limiting case of refraction and the angle of incidence is now known as the critical angle θ_c, as shown in Fig. 1.2. From (Eq 1.1) the value of the critical angle is given by:

$$\sin\theta_c = {}^{n_2}/_{n_1} \tag{1.2}$$

At angles of incidence greater than the critical angle the light is reflected back into the originating dielectric mirror, therefore total internal reflection occurs at the core-cladding interface.

Fig. 1.3 partially illustrates the transmission of a light ray in an optical fiber via a series of total internal reflection. This type of ray is the simplest to describe and is generally used when illustrating the fundamental transmission properties in optical fibers. It must also be considered that the illustrated light transmission assumes a perfect fiber, and that any discontinuities or imperfections at the core-cladding interface would likely result in refraction rather than total internal reflection.

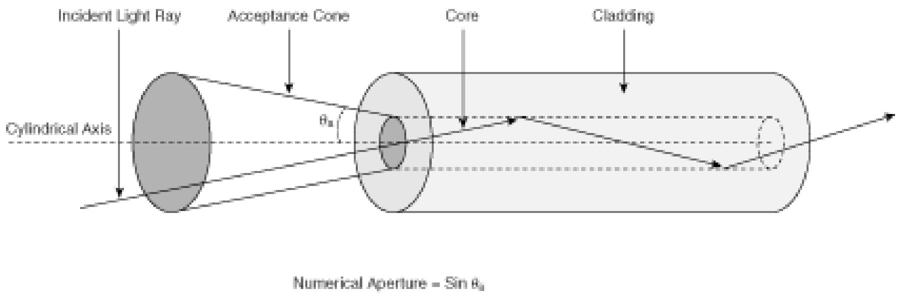

Figure 1.3 Schematic illustration of acceptance cone when launching light into the fiber

Considering the phenomena of total internal reflection, it is useful to enlarge upon the geometric optics approach with reference to light rays entering the fiber. According to the Fig. 1.3 it may be assumed that the rays entering the fiber core at an angle greater than θ_a to the fiber axis will be transmitted to the core-cladding interface at an angle less than θ_c, and will not be totally internally reflected. As a result, the rays are refracted into the cladding and eventually lost by radiation. Thus the rays to be transmitted by total internal reflection within the fiber core must be incident on the fiber core with an acceptance cone defined by the conical half angle θ_a. Hence θ_a is the maximum angle to the axis as which light may enter the fiber in order to be propagated, and is often referred as the acceptance angle for the fiber.

It is possible to obtain a relation between the acceptance angle and the refraction indices of the three media involved, namely the air n_0, core n_1 and cladding n_2. This leads to the definition of a more generally used term, the numerical aperture of the fiber (*NA*), which is defined as:

$$NA = n_0 \sin\theta_a = \sqrt{n_1^2 - n_2^2} \qquad \textbf{(1.3)}$$

Since the *NA* is often used with the fiber in air where n_0 is unity, it is simply equal to sin θ_a. It may also be noted that the incident rays over the range of $0 < \theta_1 < \theta_a$ will be propagated within the fiber [5].

So far light propagation was described as a simple ray. However, this approximation is only valid for step index multimode fibers. In order to obtain an improved model for the propagation of light in a single mode optical fiber, electromagnetic wave theory must be considered whereas the electromagnetic field propagates primarily in the fiber core and that is evanescent in the outer zone. The transition from ray to wave theory may be supported by considering a plane monochromatic wave propagating in the direction of the ray path within the guide. In this thesis, single mode optical fibers will be considered with a step profile of refractive index along the fiber radius.

$$n = \begin{cases} n_1, & r \leq a \\ n_2, & r > a \end{cases}$$

The region where $0 < r < a$ is the fiber core and the region where $r > a$ is the fiber cladding, where a is the core radius. The index of refraction of the core is slightly greater than the refraction index of the cladding. For a step index fiber, the normalized waveguide parameter V, defines the number of modes that can be guided within the fiber. V is given by

$$V = \frac{2\pi a}{\lambda} NA \tag{1.4}$$

and depends on the core radius a, the wavelength λ and the numerical aperture NA. For each wavelength λ there is a finite number of field distributions (fiber modes). They are called LP_{lm} modes (LP stands for Linear Polarized), $l = 0, 1, 2, 3, \ldots$ is a parameter of the angle ϕ dependence (in cylindrical coordinates (r, ϕ, z)) of the wave function and $m = 1, 2, 3, \ldots$ is a parameter of the different modes with the same l value. While increasing the value of l and m, the modes are poorly maintained. For $0 < V < 2.4048$ we have the situation where only one single mode is guided, usually defined as the fundamental mode. The generalized parameter $V = 2.4048$ corresponds to the cutoff wavelength λ_{cutoff}[6], given by

$$\lambda_{cutoff} = \frac{2\pi a}{2.4048} NA \tag{1.5}$$

Fibers that can guide only a single-mode radiation must therefore have a small core radius a. It is typically between 1 µm and 12 µm.

1.4 Pumping and Optical Gain

Pumping schemes for lasers can be classified in three-level or four-level schemes. Fig. 1.4 shows a diagram which can be used to explain the operation of an optically pumped three-level laser, such as Erbium ion (Er^{3+}).

In a three-level system, the laser transition ends up on the ground state. Initially all ions of the laser material are in the lowest level 1 (ground level). Excitation is supplied by radiation of frequencies which produce absorption into the level 3. Thus, the pump light raises the ions from the level 1 (ground state) to level 3. If the material is such that, after the atom has been raised to level 3, it decays rapidly to intermediate level 2 by a rapid nonradiative decay, then it enables the population inversion to occur between level 2 and 1. In this process, the energy lost by an electron is transferred to the lattice (phonons). Finally the electrons return to the ground level by emission of a photon. It is this last transition that is responsible for the laser action. Three-level systems have the characteristic that the laser transition operates between the excited laser level 2 and the final ground state 1, the lowest energy level of the system.

In four-level laser system, which is characteristic of the rare earth ions in glass or crystalline host materials, atoms are raised from the level 0 (ground level) to level 3. If the atom then decays rapidly to level 2, the population inversion can be obtained between level 2 and 1. Once the oscillation starts in such a four-level laser, the atoms will be transferred to level 1, through stimulated emission. For continuous wave operation it is therefore necessary that the transition $1 \rightarrow 0$ is very fast.

A material must possess a relaxation time τ_{10} between the terminal laser level and the ground level, fast compared with the fluorescent time τ_{21}, i.e., $\tau_{10} \ll \tau_{21}$. In addition the terminal laser level must be far above the ground state so that its thermal population is small. The thermal population of the terminal laser level 1 is determined by the relation,

$$\frac{N_1}{N_0} = exp\left(\frac{-\Delta E}{kT}\right) \tag{1.6}$$

where ΔE is the separation between level 1 and the level 0 (ground state), and T is the operating temperature of the laser material. If $\Delta E \gg kT$, then $N_1/N_0 \ll 1$, and the intermediate level 1 will be relatively empty [7][8].

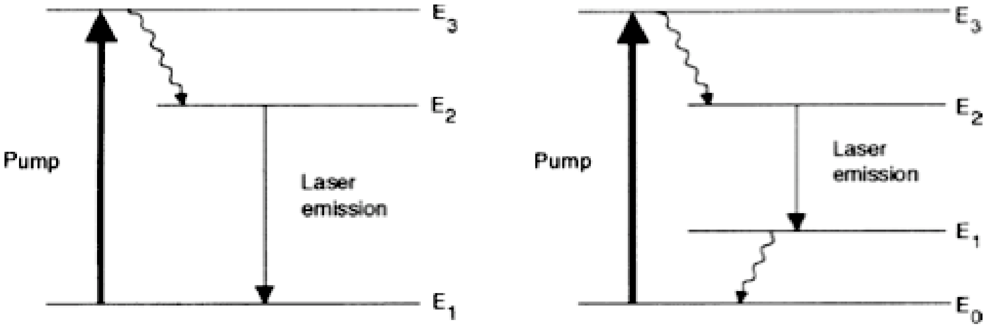

Figure 1.4 Diagram of three-level laser system on left-hand side and four-level laser system on the right-hand side. Waved arrows indicate fast relaxation of the level populations through non-radiative processes

There is also the so-called quasi-four-level laser which has become very important laser category. In this case the ground level consists in several sublevels, the lower laser level being one of the sublevels. Thus, the scheme in the right hand side of Fig. 1.4 can still be applied to a quasi-four-level laser with the understanding that level 1 is a sublevel of the ground level and level 0 is the lowest sublevel of the ground level. If one further assumes that the energy separation between levels 1 and 0 is comparable to kT, then there is always some population present in the lower laser level and the laser system behaves in such a way that is intermediate between a three- and a four-level laser [4].

The major dopants currently employed for fiber lasers are Ytterbium (Yb^{3+}), Neodymium (Nd^{3+}) and Erbium (Er^{3+}). Ytterbium provides a quasi-four-level system and is often used for high-power lasers operating near 1.01 μm. In common with the Nd: YAG laser, Nd^{3+} provides a four-level scheme with significant laser outputs at wavelengths of 0.90 μm, 1.06 μm and 1.32 μm. On the other hand, the element Erbium provides a three-level scheme with the most relevant lasing transition at 1.55 μm. One consequence of the number of levels involved in the laser action that is of particular significance to fiber lasers is the length dependence of the threshold power. Assuming that the imperfections losses are low, then in a four-level system the threshold power decreases inversely with the gain medium length. In a three-level system, however there is an optimum length that gives the minimum threshold power which is independent of the value of the imperfection losses [5].

1.5 Laser Threshold and Gain Coefficient

The two most important parameters characterizing a laser are the threshold pump power and the efficiency with which the laser converts the pump power into laser power once it has reached the threshold. Laser threshold is determined by the need of the gain to compensate cavity losses during each round trip. Considering the most simple cavity design, formed by placing two mirrors of reflectivity R_1 and R_2 at the two ends of the fiber of length L, the threshold condition becomes

$$G^2 R_1 R_2 \exp(A) = 1 \tag{1.7}$$

where G is the single-pass amplification factor and A corresponds to intracavity losses per length. Due to the nonuniform nature of the gain coefficient, the single-pass amplification factor must include the following equation,

$$G = exp\left[\int_0^L g(z)d(z)\right], \qquad g(z) = \sigma_s[N_2(z) - N_1(z)] \tag{1.8}$$

where $g(z)$ corresponds to the gain coefficient as a function of the distance z along the fiber, σ_s is the transition cross section and N_1 and N_2 are the dopant densities in the two energy states participating in the stimulated emission process.

The population inversion depends on the pumping strength. In the general case, it is calculated by using a set of three or four rate equations for the energy levels involved in the pumping process. Considering a three-level system, and assuming the pump level remains almost unpopulated due to the rapid transfer of the pumped population to the excited state, the excited density $N_2(z,t)$ is obtained by solving the following rate equation,

$$\frac{\partial N_2}{\partial t} = W_p N_1 - W_s(N_2 - N_1) - \frac{N_2}{T_1} \tag{1.9}$$

where $N_1 = N_t - N_2$, N_t is the total ion density, T_1 is the relaxation time, and W_p and W_s are the transition rates for the pump and signal, respectively. These rates are given by

$$W_p = \frac{\Gamma_p \sigma_p P_p}{a_p h\upsilon_p}, \qquad W_s = \frac{\Gamma_s \sigma_s P_s}{a_s h\upsilon_s} \tag{1.10}$$

where Γ_p stands for the overlap factor representing the fraction of pump power P_p within the doped region of the fiber, σ_p is the transition cross section at the pump frequency ν_p, and a_p is the mode area of the pump inside the fiber. The same quantities are similarly defined for signal.

Considering a four-level system, the calculation gets simpler since $N_1 \approx 0$ and $N_2 << N_t$, therefore the equation turns into,

$$\frac{\partial N_2}{\partial t} = W_p N_t - W_s N_2 - \frac{N_2}{T_1} \tag{1.11}$$

The steady-state solution is given by

$$N_2 = \frac{(P_p/P_p^{sat})N_t}{1 + P_s/P_s^{sat}} \tag{1.12}$$

where the saturation powers are defined in the following equation,

$$P_p^{sat} = \frac{a_p h\upsilon_p}{\Gamma_p \sigma_p T_1}, \qquad P_s^{sat} = \frac{a_s h\upsilon_s}{\Gamma_s \sigma_s T_1} \tag{1.13}$$

The *z* dependence of N_2 follows from variations in the pump and signal powers along the cavity length [1].

1.6 Cavity Design

Fiber lasers can be designed with a variety of choices for the laser cavity. The most common laser configuration is Fabry-Pérot cavity (Fig. 1.1), which is typically formed by placing the gain medium between two high reflective mirrors in contact with the ends of the doped fiber, which are either polished or cleaved perpendicular to the fiber axis. The reflector at the pump input end permits coupling of the pump light into the cavity while retaining a high reflectivity at the laser wavelength. A variation of this design uses dielectric reflectors placed directly onto the polished ends of the doped fiber. However, end-coated mirrors are quite sensitive to imperfections at the fiber tip.

One alternative consists in using fiber couplers which have the advantage of avoiding passing the pump light through the dielectric mirror and therefore enables that most of the pump power comes out of the port that is a part of the laser cavity. Such couplers are called as *Wavelength division multiplexing* (WDM) couplers.

Another simple setup consists in a fiber with fiber Bragg gratings at both ends that can act as a high reflectivity mirror for the laser wavelength while transmitting pump radiation. A pigtailed pump diode is spliced to one fiber end whereas the other end delivers the laser radiation. The use of two such gratings results in an all-Fabry-Perot cavity. An additional advantage of Bragg gratings is that the laser can be forced to operate in a single longitudinal mode [1][4].

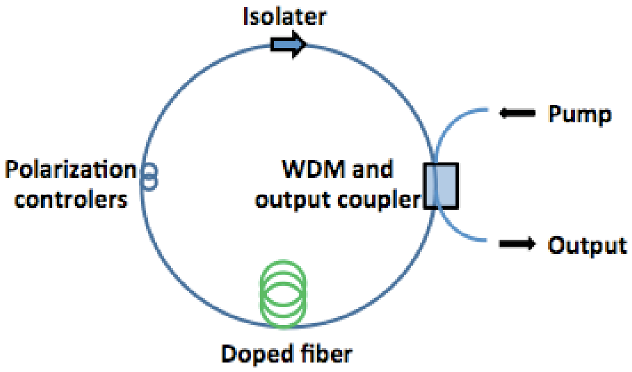

Figure 1.5 Schematic illustration of a unidirectional ring cavity used for fiber lasers.

Other important fiber lasers are ring lasers. They are relatively easy to produce, in practice by forming an optical loop including the doped fiber. Ring cavities are often used to realize unidirectional operation of a laser. A major advantage is that the ring cavity can be made without using mirrors, resulting in an all-fiber cavity [1][2]. In the simplest design, two ports of a WDM coupler are connected together to form a ring cavity containing the doped fiber (Fig. 1.5). An isolator is inserted within the loop for unidirectional operation. A polarization controller is also required for conventional doped fiber that does not preserve polarization [9].

1.7 Short Pulses Fiber Lasers

In many applications it is useful to operate lasers in a pulse mode. Two techniques used for generating short optical pulses from lasers are known as *Q-switching* and *mode locking*.

1.7.1 Q-Switching

Diode lasers although convenient and compact, are inherently poor because the damage thresholds of semiconductor materials are low. Glass on the other hand, supports high optical intensities without damage. Direct modulation of a fiber laser in the form of Q-Switching allows generation of significant peak powers and short duration pulses [6]. The generation of a Q-switched pulse basically modulates the intracavity losses and thus the “Q” factor (quality factor of the optical resonator). It can be described by keeping the resonator losses at a high level (producing an optical resonator with low Q), so that the lasing cannot occur. As a result the energy fed into the gain medium by the pumping mechanism is accumulated. The amount of energy stored in the gain medium increases as the gain medium is pumped. After a certain time, the stored energy will reach the order of the maximum level of the gain medium and thus the gain starts to be saturated. At this point, the losses are suddenly reduced to a small value (the Q factor is rapidly restored to its high value), so that the power of the laser radiation builds up very quickly in the laser resonator. The large intracavity power present at that time leads to further depletion of the stored energy during the time where the power decays. The net result is a short pulse of light output from the laser, known as a *giant pulse*, which is typically in the nanosecond range, corresponding to the several cavity round trips. The peak power can be orders of magnitude higher than the power that is achievable in cw operation.

The major difference between Q-switching in fiber lasers and in other miniature lasers is the high single-pass gain often encountered in the fiber geometry. As a result, the pump power requirement is reduced, but also modulators for Q-switching must have a high extinction ratio. This is one of the major factors limiting the achievement of increased output of Q-switched fiber lasers [7][8].

Q-switching produces relatively broad optical pulses (~100 ns). In contrast, mode locking can generate pulses shorter than 100 fs. Q-switching leads to much lower repetition rates (500 Hz), much higher pulse energies (> 2 mJ) and much longer pulse durations comparing with mode locking [1].

Q-switched lasers are often used in applications which demand high laser intensities in nanosecond pulses, such as metal cutting or pulsed holography. Nonlinear optics often takes advantage of the high peak powers of these lasers, offering applications such as 3D optical data storage and 3D microfabrication.

1.7.2 Mode Locking

For applications such as electro-optic sampling, range finding, and telecommunications, there is a need for pulses with a shorter duration than those available from Q-switched lasers. These short pulses, generally referred as ultrafast pulses, can be generated in a laser source through the coherent process known as mode locking [9].

Fiber lasers operate simultaneously in a large number of longitudinal modes falling within the gain bandwidth. The frequency spacing among the modes is given by $\Delta\nu = c/L_{opt}$ where L_{opt} is the optical path during one round trip inside the cavity. Multimode operation is due to a wide gain bandwidth compared with relatively small mode spacing for fiber lasers ($\Delta\nu \sim 10$ MHz) [1].

Mode locking techniques can be classified in passive or active. Active mode locking requires the help of an external modulated media or device, in contrast, passive mode locking enables to initiate mode locking based on the exploitation of an optical effect in a material without any time varying intervention [10].

1.7.2.1 Active Mode Locking

Active mode locking is essentially achieved by modulating either the amplitude or the phase of the intracavity optical field at a frequency f_{m} equal or multiple of the mode spacing $\Delta\nu$. It is referred to as *AM* (amplitude modulation) or *FM* (frequency modulation) mode locking depending on whether amplitude or phase is modulated. Both *AM* and *FM* techniques generate modulation sidebands, spaced apart the modulation frequency f_{m}. These sidebands overlap with the neighboring modes when $f_{\mathrm{m}} \approx \Delta\nu$. Such an overlap leads to phase synchronization. The mode locking process can be modeled by using a set of multimode rate equations in which the amplitude of each mode is coupled to its nearest neighbors [1].

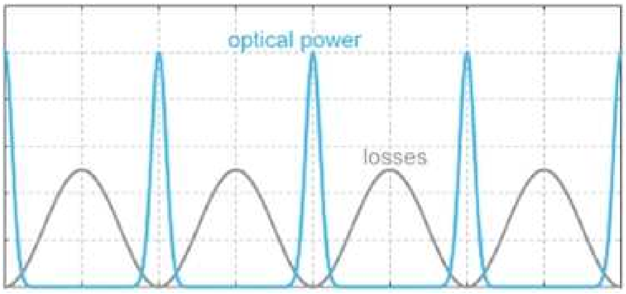

Figure 1.6 Schematic illustration of active *AM* mode locking through modulation of cavity losses. The blue line represents the mode locked pulses, and the grey line represents the modulated cavity losses.

Fig. 1.6 shows the case of *AM* mode locking. The laser cavity loss is modulated periodically at the round trip time at the frequency $\Delta\nu$. Since the laser produces more intensive light when the losses are minimum, it is favorable for the intracavity field to consist of a short optical pulse circulating inside the laser, which passes through the modulator at the points of maximum transmission. The difference of intensity builds up on successive round trips, and the laser emits a train of mode-locked pulses in the steady state.

In the frequency domain it is assumed that the modulator produces sidebands to each of the oscillating axial modes at the axial-mode spacing, which tends to lock the modes of the laser in phase. The width of the generated pulses is then approximately given by T / N, where T is the cavity round trip time and N is the number of axial cavity modes mode-locked by the modulator.

In the case of FM mode locking, the phase is modulated at the cavity round trip time, which also leads to pulses much shorter than the modulation period with an associated frequency equal to the time derivative of the phase modulation.

In order to achieve the process, it is required to employ an acousto-optic or electro-optic modulator, a Mack Zehnder integrated optic modulator, or a semiconductor electro-absorption modulator [9].

1.7.2.2 Passive Mode Locking

Passive mode locking is an all-optical nonlinear technique capable of producing ultrashort optical pulses, without requiring any active component (such as a modulator) inside the laser cavity. It makes use of a nonlinear device whose response to an entering optical pulse is intensity dependent such that the exiting pulse is narrower than the input pulse.

Saturable Absorbers

Pulse shortening provides a mechanism through which a laser can minimize cavity losses by generating intense pulses if the cw radiation is unable to saturate the absorber. In the pulse formation process, the saturable absorber enhances fluctuations induced by spontaneous emission during multiple round trips within the laser cavity until a certain intense pulse reaches the saturation of the absorber. The pulse shortness reaches its limit when its spectral width is comparable to the gain bandwidth. The reduced gain in spectral wings then provides the broadening mechanism that stabilizes the pulse width to a specific value. In the case of fiber lasers, GVD (Group Velocity Dispersion) and SPM (Self Phase Modulation) also play an import role in evolution of mode-locked pulses and should be included. Several implementations of this basic idea have been used to make passively mode-locked fiber lasers [1].

Passive mode locking (with a saturable absorber) permits the generation of shorter pulses, because a saturable absorber, driven by already short pulses, can modulate the resonator losses much faster than an electronic modulator.

Nonlinear Fiber-Loop Mirrors

The implementation of nonlinear fiber-loop mirrors (NFLM) or Sagnac Interferometers has created a lot of attention due to its capability of power-dependent transmission which allows to shorten an optical pulse just like saturable absorbers do, however with the advantage that the fiber lasers do not loose their all-fiber nature. This system is referred to as figure-8 lasers because of its appearance of their cavity (Fig. 1.7). The laser consists of two fiber loops connected by a 2 x 2 central coupler, which splits the entering radiation into two equal counter-propagating parts. The left-hand loop in the figure contains an insulator that ensures unidirectional operation. The polarization controllers are used to bias the polarization of the circulating light appropriately with respect to the small and essentially random birefringences present in normal circular-core single-mode fibers.

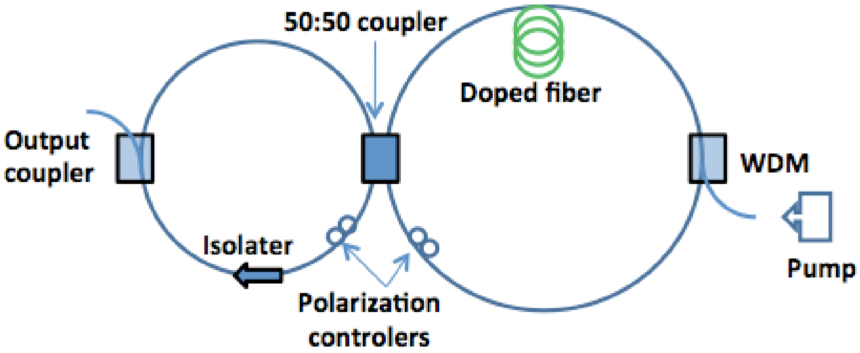

Figure 1.7 Schematic illustration of a figure-8 cavity useful for mode-locked fiber lasers

The right-hand loop is referred as nonlinear amplifying loop mirror (NALM). This loop contains a doped fiber close to the central coupler in order to provide amplification such that one wave is amplified at the entrance to the loop while the other experiences amplification just before exiting the loop. The counter propagating waves during a complete round trip inside the NALM acquire different nonlinear phase shifts. Moreover, the phase difference is not constant but varies along the pulse profile. If the NALM is adjusted such that the phase shift is close to π for the central intense part, this part of the pulse is transmitted, while pulse wings get reflected because of their lower power levels and smaller phase shifts. This leads to an exiting pulse narrower compared with the one entering it. Because of this property, a NALM behaves similarly to a fast saturable absorber except for one major difference: it is capable of responding at femtosecond timescales because of the electronic origin of the fiber nonlinearity [1][11][12].

1.8 Erbium-Doped Fiber Laser (EDFL)

Fibers doped with erbium have been extensively studied in the past few years for their potential as amplifiers for telecommunication systems. They have produced sources with a broad range of properties, including narrow line width and tunable emission, femtosecond mode-locked lasers and broadband sources. They can operate in several wavelength regions, ranging from visible to infrared regime. The 1550 nm wavelength acquires the most attention due to the coincidence with the low-loss region of silica fibers used for optical communications.

In most materials, e.g., optical fiber, erbium assumes the trivalent charge state (Er^{3+}) with an electronic configuration of $[Kr]\cdot 4d^{10}\cdot 4f^{11}\cdot 5s^2\cdot 5p^6$. Spin-spin and spin-orbit coupling in the incompletely filled 4f shell give rise to a number of energy levels. Each degenerate level is Stark-split into a manifold of levels, due to the presence of the host material [13]. The transition from the first excited state ($^4I_{13/2}$) to the ground state ($^4I_{15/2}$) occurs at a wavelength of approximately 1540 nm. The emission wavelength is relatively insensitive to the host material, because the 4f shell is shielded from its surroundings by the filled 5s and 5p shells.

EDFL can operate at 1550 nm with most efficiency by pumping at 980 nm and 1480nm, due to the inexistence of excited state absorption. Both wavelengths have been used for developing practical EDFLs with excellent performance features and the choice between the pump wavelengths is not always clear since each pumping wavelength has its own merits [1].

The three energy level scheme is quite successful in explaining the properties of EDFLs and has been used to analyze the optimal design for EDFLs. $^4I_{15/2}$, $^4I_{13/2}$, and $^4I_{11/2}$ are known as the ground state, the metastable state and the excited state, respectively. Metastable state means that this level has a very long lifetime of 10 ms compared to other downward transitions. N_1, N_2 and N_3 are the population of electrons in the respective energy levels. Erbium ions are pumped to an upper energy level by the absorption of light from the pump source at either 980 nm or 1480 nm [14].

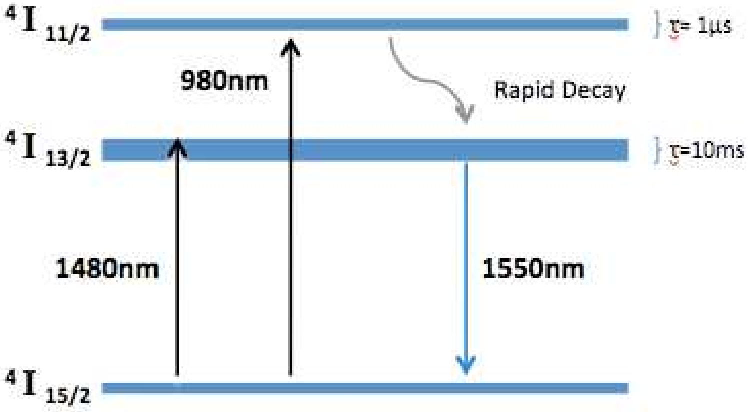

Figure 1.8 The three-level energy diagram of erbium ions.

The laser transition where the highest gain occurs is the $^4I_{13/2} \rightarrow {}^4I_{15/2}$, which is centered at 1540 nm. It terminates on the ground state manifold $^4I_{15/2}$, and it is therefore essentially a three level transition. However this manifold is broad enough to permit longer wavelength transitions ($\geq$ 1600 nm) to terminate on the less populated upper levels of the manifold and to be quasi-four-level transitions. Several pump bands are available to populate the upper state $^4I_{13/2}$. The bands relevant to pumping with semiconductor laser diodes are shown in the energy level diagram in Fig. 1.8.

1.8.1 Pump Wavelengths

Erbium doped fiber lasers can be distinguished based on their pump wavelength, a parameter that strongly affects their performance.

The pumping near 800 nm by GaAs semiconductor lasers has been a strong incentive to investigate EDFL despite the relatively strong pump ESA (Excited state absorption).

In attempt to produce more efficient sources, fiber lasers have been made with fibers codoped with ytterbium. Such EDFLs have a ratio of ytterbium and erbium concentrations of more than 20 and can be pumped using 800 nm semiconductor lasers or miniature 1060 nm Nd:YAG lasers. The improved performance of Yb-sensitized EDFLs is due to the near coincidence of the $^2F_{5/2}$ state of Yb^{3+} ions with the $^4I_{11/2}$ state of Er^{3+} ions. The absorption of a pump photon by a Yb^{3+} ions promotes an electron from the $^2F_{7/2}$ ground state level to the $^2F_{5/2}$ manifold, which is followed by efficient energy transfer from this level to the $^4I_{11/2}$ level of erbium and nonradiative decay to the upper level $^4I_{13/2}$. The lasing occurs down to the $^4I_{15/2}$ manifold. Laser action terminates at a Stark level within the ground manifold. At room temperature all levels of the terminal $^4I_{15/2}$ manifold are populated to some degree, thus this transition forms a quasi-four-level laser scheme with a correspondingly high threshold.

Although much progress has been achieved in 800 nm pumped EDFLs, the performance of these devices is still limited by the presence of pump ESA. On the other hand the pumping wavelength 980 nm enables the operation of the region free of ESA. An additional property consists on the fact that laser diodes in this range with reasonable lifetimes are commercially available and practical pump sources. The main characteristic of this wavelength, for high pump powers, is that it exhibits the highest gain and thus the threshold of fiber lasers pumped at this wavelength is expected to be as low as possible.

The pumping wavelength 1480 nm is as well able to provide a region free of ESA, however since the pumping wavelength is very close to the laser wavelength, the maximum, quantum-limited slope efficiency of the laser, equals to the ratio of laser to pump photon energies is expected to be higher for 1.48 μm pumping than 980 nm, by a factor of $1.48/0.98 \approx 1.5$. On the other hand, the gain for erbium-doped fibers is generally smaller with 1480 nm than with 980 nm. Therefore the threshold of 1480 nm pumped fiber lasers is expected to be higher. A disadvantage for pumping at 1480 nm, stimulated emission at this wavelength reduces the maximum achievable population inversion [8][9].

1.8.2 Fiber Length

In the three-level fiber lasers, the fiber length indeed plays an important role, as it affects the threshold, the slope efficiency, and the wavelength of the fiber. Firstly, in an EDFL any length of unpumped fiber acts as a strong absorber at the wavelength and increases the threshold. Therefore for a given set of fiber and pump parameters, exists an optimum length that minimizes the threshold. Moreover, with the increasing of the fiber length, the amount of pump power absorbed by the fiber is increased as well, and therefore increases the slope efficiency with respect to the pump power.

In general, the length that maximizes the output power is different from the length that minimizes the threshold, and this length obviously depends on the available pump power.

2 Laser Spectroscopy

Spectroscopy has made a remarkable contribution to the current state of atomic and molecular physics, to chemistry and molecular biology. Information on molecular structure and on the interaction of molecules with their surrounding may be derived in various ways from the absorption or emission spectra generated when electromagnetic radiation interacts with matter.

Each atom or molecule is characterized by a set of energy levels. Transitions between levels by absorption or emission of electromagnetic radiation result in highly specific spectroscopic features. These features allow identification and quantification of the molecular species. Molecules may experience transitions between electronic, vibrational and rotational states when exposed to electromagnetic radiation, resulting in absorption spectra. These spectra consist of a number of discrete absorption lines. Each line has a certain linewidth and shape that depends on temperature and what surrounds the molecule.

Wavelength measurements of spectral lines allow the determination of energy levels of the atomic or molecular system. The line intensity is proportional to the transition probability, which measures how strongly the two levels of a molecular transition are coupled. The natural linewidth of a spectral line may be resolved directly with a spectrometer, allowing mean lifetimes of excited molecular states to be determined. Time-resolved measurements allow the spectroscopist to keep up with dynamical processes in ground- and excited-state of molecules, to investigate collision processes and various energy transfer mechanisms. Laser spectroscopic studies of the interaction of single atoms with a radiation field provide accurate tests of quantum electrodynamics [15].

2.1 Basic Foundations

In order to understand basic considerations regarding absorption and emission of electromagnetic radiation interacting with matter, we may start to discuss some aspects concerning thermal radiation fields and the concept of cavity mode. According to the *black body radiation* theory, an object or system which absorbs all radiation incident upon it, re-radiates energy which is characteristic of this radiating system only. The radiated energy can be considered to be produced by standing wave or resonant modes of the cavity which is radiating. The amount of radiation emitted in a given frequency range should be proportional to the number of modes in that range. The number of modes per unit volume within the frequency interval dν is given by [15],

$$n(\nu)d\nu = \frac{8\pi\nu^2}{c^3}d\nu\,. \tag{2.1}$$

From the assumption that electromagnetic modes in the cavity are quantized in energy with the quantum energy equal to Planck’s constant times the frequency, a radiation formula is derived [15]. The mean energy $\langle E\rangle$ per modes is given by,

$$\langle E\rangle = \frac{h\nu}{e^{h\nu/\kappa T}-1}\,. \tag{2.2}$$

The thermal radiation field has the energy density $\rho(\nu)\,d\nu$ within the frequency interval ν to $\nu + d\nu$, which is equal to the number $n(\nu)\,d\nu$ of modes in the interval dν times the mean energy per mode. According to (Eqs. 2.1, 2.2) one obtains

$$\rho(\nu)d\nu = \frac{8\pi\nu^2}{c^3}\frac{h\nu}{e^{h\nu/\kappa T}-1}d\nu\,. \tag{2.3}$$

This is Planck's famous *radiation law*, which predicts a spectral energy density of the thermal radiation that is fully consistent with experiments. The expression "thermal radiation" comes from the fact that the spectral energy distribution (Eq. 2.3) is characteristic of a radiation field that is in thermal equilibrium with its surroundings.

The spectral distribution of the radiant flux from a source is called emission spectrum. The thermal black body radiation has a continuous spectral distribution described by its spectral energy density (Eq. 2.3). Discrete emission spectra, where the radiant flux has distinct maxima at certain frequencies ν_{ik}, are generated by transitions of electrons in atoms or molecules between two bound states, a high energy state E_k and a low energy state E_i, according to the following relation,

$$h\nu_{ik} = E_k - E_i\,. \tag{2.4}$$

If radiation with a continuous spectrum passes through a gaseous molecular sample, molecules in the lower state E_i may absorb radiant power at the eigenfrequencies $\nu_{ik} = (E_k - E_i)/h$, which is thus missing in the transmitted power. The difference in the spectral distributions of incident minus transmitted power is the *absorption spectrum* of the sample. The absorbed energy $h\nu_{ik}$ brings a molecule into the higher energy level E_k. If these levels are bound levels, the resulting spectrum is a discrete absorption spectrum. If E_k is above the ionization energy, the absorption spectrum becomes continuous. Examples of discrete absorption lines are the Fraunhofer lines in the spectrum of the sun, they are produced by atoms in the sun's atmosphere that absorb at their specific eigenfrequencies the continuous blackbody radiation from the sun's photosphere [15][16].

2.2 Width and Profile of Spectral Lines

Spectral lines of discrete absorption and emission spectra have a nonzero linewidth. Even with the very high resolution spectrometer, one can observe a spectral distribution $I(\nu)$ of the absorbed or emitted intensity around the central frequency $\nu_0 = (E_i - E_k)/h$ corresponding to a molecular transition with the energy difference $\Delta E = E_i - E_k$ between upper and lower levels. The distribution $I(\nu)$ is called the *line profile* (Fig. 2.1). The frequency interval $\Delta\nu = |\nu_2 - \nu_1|$ between the two frequencies ν_1 and ν_2 for which $I(\nu_1) = I(\nu_2) = I/2(\nu_0)$ is the *full width* at *half maximum* of the line (FWHM).

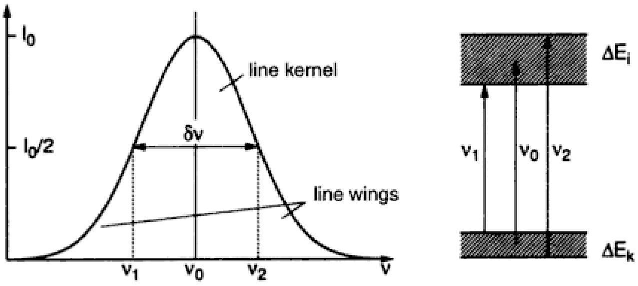

Figure 2.1 Schematic illustration of a spectral line profile

The spectral region within this interval is called the *Kernel of the line*, while the regions outside ($\nu < \nu_1$ and $\nu > \nu_2$) are the *line wings*.

The spectral lines are broadened because the energy levels are not infinitely sharp and due to the motion of the atoms. The natural broadening, collision broadening and thermal or Doppler broadening are three main mechanisms that determine the line profiles of gaseous media. The uncertainty principle relates the lifetime of an excited state due to the spontaneous radiative decay with the uncertainty of its energy with resulting in natural line broadening. The collisions reduce the effective lifetime of a state, leading to broader lines. Thermal or Doppler broadening also influences the profile of spectral lines due to the thermal motion of absorbing or emitting molecules [15][16].

2.3 Absorption Spectroscopy

Absorption spectroscopy is a high-resolution and high sensitive technique capable of detection and characterization of multicomponent gaseous samples. It is commonly used for various diagnosis purposes, such as environmental, combustion and plasma research, and in medicine and stable isotope ratio measurements [17].
The technique is based on the measurement of the spectral extinction, by the absorber, of light transmitted through the sample. The light intensity I decreases along the distance dl by [15],

$$dI = -\kappa(v) I dl\,. \tag{2.5}$$

The solution of this equation is Lambert-Beer law (Eq. 2.6), which relates the absorption of light to the properties of the material through which the light is traveling.

$$I(v) = I_0(v)\exp\left[-\kappa(v)L\right] \tag{2.6}$$

This law states that there is a exponential dependence of the light transmission through the material, where $I_0(v)$ is the intensity of the incident spectral light flux, $I(v)$ is the intensity of the transmitted light flux, $\kappa(v)$ (cm^{-1}) is the absorption coefficient of the sample, and L is the optical path length of the absorber. The absorption coefficient is determined by the absorber density n and the transition cross section σ (cm^2) by,

$$\kappa(v) = n\sigma(v)\,. \tag{2.7}$$

The absorption signal K in the transmitted spectrum is defined as

$$K = \ln {}^{I_0}\!/_{I}\,, \tag{2.8}$$

for a small absorption signal, $\Delta I \ll I_0$,

$$K = \Delta I / I_0 \tag{2.9}$$

with ΔI being the reduction of the light flux by the absorption. The detection limit is defined as the smallest absorption coefficient κ_{min} detected in the transmitted spectrum. It is characterized by the signal-to-noise ratio in the recorded spectrum, and by the absorption path length, L. The absorption path length can be increased by using a long free propagation of light in the atmosphere, or by folding the light beam in a multireflective cell [18]. Free propagation of light in the atmosphere was obtained with 16 km absorption length [19]. Such long-path measurements, however, apply only to atmospheric extinction and simply provide and average over the entire absorber length. Multireflective cells enable some 100-fold increase of the effective absorption length. This factor is limited by the loss of light at the mirrors, and by the requirement of sufficient geometrical separation of the successively reflected laser beams. With 10 m base length of the cell, the effective absorption length may be up to 1 km. The detection limit is determined in the following way,

$$\kappa_{min} = \frac{(K)_{min}}{(L)_{max}}, \tag{2.10}$$

where $(K)_{min}$ is the noise-equivalent absorption signal, and $(L)_{max}$ is the maximum value of absorption path length.

A long effective absorption path can be realized if the sample is placed inside a passive high-finesse cavity, e.g., by cavity ringdown spectroscopy (CRDS) [20][21]. Here the absorber is placed inside a passive cavity, into which a short laser pulse is injected. From the measured decay time of this pulse, which is determined by the ratio of the total cavity loss and the cavity round-trip time, the absorption is derived. The absorption path length is determined by the average number of round trips of the light, which is limited by the selection of high reflective mirrors, and by the cavity length L. A cavity finesse used for CRDS is frequently as high as 10^5. The finesse of an optical cavity influences the enhancement factor for the intracavity absorption signal that can be recovered from the cavity transmission. In contrast with CRDS, intracavity laser absorption spectroscopy does not require a high finesse cavity [22]. Very high spectral sensitivity is obtained by intracavity absorption spectroscopy (ICAS) with a multimode laser whose homogeneously broadened gain exceeds the absorption linewidth. In such a multimode laser, the broadband cavity loss is compensated by the laser gain. This laser is equivalent to an undamped cavity with extremely high finesse, 10^5 – 10^{10}, even if the reflection of the output mirror in the laser cavity is only 50%. This finesse is limited by the duration of laser oscillations or by perturbations of the light coherence, e.g., by spontaneous emission. The principal requirement for intracavity absorption measurements of high sensitivity is that the line width of the absorber is smaller than the homogeneous spectral broadening of the gain medium. In this case the laser gain compensates broadband cavity losses such as the mirror transmission, but not the narrow-line intracavity absorption [22].

Various lasers such as, dye, solid state and fiber lasers have been successfully used for intracavity absorption measurements of gaseous samples whose linewidth are typically less than 0.3 cm^{-1}. So far, the highest sensitivity with to intracavity absorption has been achieved with a dye laser, where effective absorption path lengths of up to 70.000 km have been demonstrated in the visible spectral range [23].

2.4 Intracavity Absorption Spectroscopy

The principal features of intracavity absorption spectroscopy (ICAS) with multimode lasers are shown in Fig. 2.2. The laser cavity consists of a HR (high reflective mirror) and OC (output coupling mirror), and includes a medium of broadband gain $G(\upsilon)$ and a sample with a narrow-line absorption spectrum $\kappa(\upsilon)$. The sample may be confined in an absorption cell, or just placed in an open part of the cavity. Although the laser gain is made to compensate broadband cavity loss such as the mirror transmission, it is not affected by narrow-line ICA. With the absorber directly placed within the cavity, the laser light passes back and forth through the absorber many times. Absorption signal will be amplified by the multiple passes and will appear superimposed on the broad spectrum of the laser. If the absorber linewidth equals or even exceeds the homogeneous gain broadening, the spectral sensitivity of ICA measurements is much lower. This case is equivalent to single-mode intracavity laser [22].

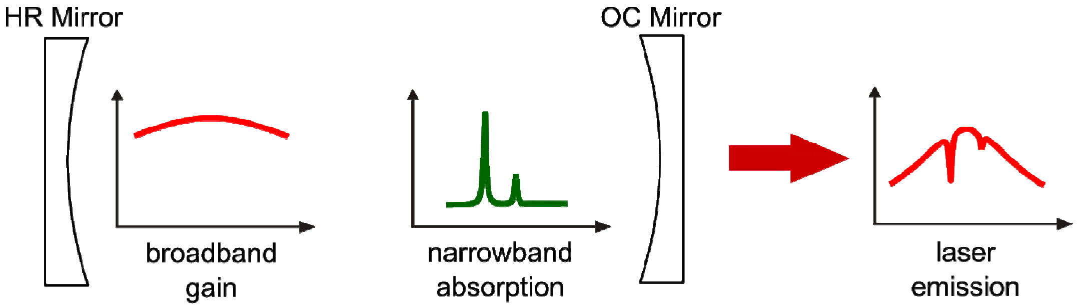

Figure 2.2 Schematics of measurements of intracavity absorption

Tuning the broadband laser emission to a specific spectral region is accomplished by wavelength selective elements in the cavity, such as a prism, a lens with chromatic aberration, or a pellicle, by using specially coated cavity mirrors, or by adjusting the parameters of the laser operation and the cavity configuration. Optical elements yield spectral periodic loss due to interference effects by light reflected and scattered. Therefore the cavity must be design in such a way to reduce these losses, for instance, avoid optical components inside the laser with parallel or nearly parallel surfaces. Due to the high sensitivity of the laser emission to intracavity extinction, scattering on dust particles or imperfections of intracavity optical surfaces may be large enough to cause parasitic etalon fringes in the laser output spectrum. In attempt to avoid etalon fringes, the laser mirrors must be made of thick substrates with their back surfaces tilted by 5° to 10°. Optical windows inside the cavity have to be thick and wedged. Light reflected or scattered from etalons outside the cavity may re-enter the cavity through the output mirror and thus create etalon fringes in the laser output. The use of a unidirectional ring laser may also result in reducing the spectral modulation of loss. The emission spectrum of the laser is normally measured with a grating spectrograph and a multichannel recorder, for example, a diode array or a photographic plate [17][22].

2.4.1 Spectral Characteristics of Laser Emission

The frequency spectrum of a laser is determined by the spectral range of the active laser medium, i.e., its gain profile, and by the resonator modes falling within this spectral gain profile (Fig. 2.3).

All laser modes for which the gain exceeds the losses can participate in the laser oscillation. The frequency maximum is determined by the laser mode, q_{max}, which has the largest net gain (difference between gain and losses). For a homogeneously broadened gain medium, each excited ion can simultaneous contribute to the gain of all the modes above threshold and with frequencies within the homogeneous linewidth of the laser. For an inhomogeneous broadened gain medium, all laser modes within the gain profile above threshold can oscillate simultaneously, but different laser modes cannot obtain gain from the same ion. The line profile of an inhomogeneous broadened laser transition can be divided into homogeneously broadened subsections of frequency intervals. Only the molecules in the upper laser level that belong to that section can contribute to the amplification of the laser wave. A monochromatic wave therefore causes selective saturation of this subgroup and burns a hole into the homogeneous distribution [15][16].

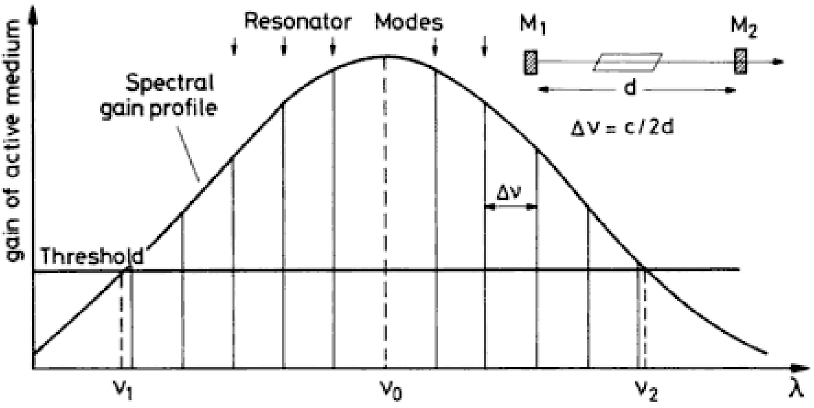

Figure 2.3 Schematic illustration of the spectral gain profile of a laser transition. The vertical lines represent the longitudinal modes of the laser cavity. The central dashed line at frequency ν_0 indicates the mode with highest gain. The dashed lines at frequencies ν_1 and ν_2 represent the limit whereas the mode intensity reaches the threshold. M_1 and M_2 are indicated as cavity mirrors, *d* as cavity length and *c*, as speed of light

Many properties of multimode lasers and, in particular, the temporal evolution of their emission spectrum and the response to intracavity absorption are reasonably described by rate equations for the mean values of photon numbers Mq in the laser mode q, and for the laser inversion N.

Assuming the gain is homogeneously broadened, and accounting that the laser operates in a four-level system, the rate equations for such a laser are given by [18],

$$\dot{M}_q = -\gamma M_q + B_q N\left(M_q + 1\right) - \kappa_q c M_q \tag{2.11}$$

$$\dot{N} = P - AN - N \sum_q B_q \, M_q \, . \tag{2.12}$$

Where, γ is the broadband cavity loss, κ_q is the absorption coefficient for intracavity absorption at the q-th axial laser mode, c is speed of light, P is the pump rate, and A is the rate of spontaneous decay of the upper laser level. Laser inversion equals the population N of the upper laser level. From the rate equations, an equation that describes the evolution of the laser with intracavity absorption present can be derived,

$$M_q(t) = M_{q_0} \frac{\sqrt{\frac{\gamma t}{\pi}}}{Q} \exp\left[-\left(\frac{q - q_0}{Q}\right)^2 \gamma t\right] \exp(-\kappa_q c t) \tag{2.13}$$

where Q is the spectral width of the Lorentzian gain profile (FWHM). This equation consists in two exponential terms. The first describes the broad Gaussian shape of the laser and accounts for the spectral narrowing of the gain profile with the width (FWHM), $\Delta q(t) = Q(\ln 2 \,/\gamma t)^{1/2}$. The second exponential can be recognized as the Beer-Lambert law, accounting for the profile of any narrowband absorber introduced within the cavity.

The ratio of the sample cell length to the total cavity length is called the filling factor. Fig. 2.4 illustrates the time evolution of an ICAS experiment. The narrowing of the spectral output of the laser is a result of the competition between the longitudinal modes of the laser.

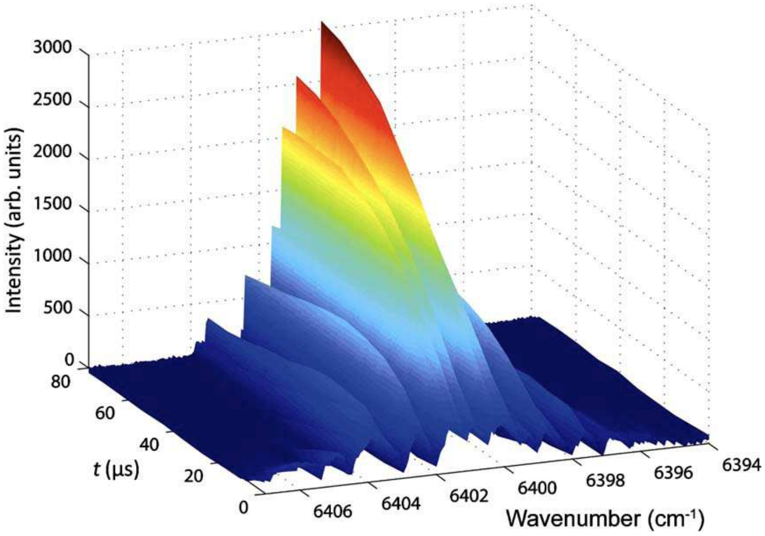

Figure 2.4 Spectral dynamics of the emission of Er^{3+}-doped fiber laser

The absorption signal in the emission spectrum initially increases with the duration of the laser emission, and finally saturates to its stationary spectral shape. According to (Eq. 2.8), the value of absorption signal Kq in the initial stage of laser emission in mode q is

$$K_q = \ln \frac{M_q}{M_{q,\kappa}} = \kappa_q ct \tag{2.14}$$

where the number of photons in mode q is $M_{q,\kappa}$ in the presence of intracavity absorption, and M_q in the absence.
The mean stationary mode distribution of the photon numbers in the laser with ICA is calculated from the stationary inversion, which is derived from (Eq. 2.11) at $\dot{M} = 0$:

$$M_{q,\kappa}^s = \frac{M_q^s}{1 + \frac{c\kappa_q M_q^s}{\gamma}} \tag{2.15}$$

With this result, the stationary absorption signal in mode q is

$$K_q^s = \ln\left(1 + \frac{\kappa_q c M_q^s}{\gamma}\right) \tag{2.16}$$

When absorption is week, such that $K^s << 1$, the equation becomes,

$$K_q^s \cong \frac{\kappa_q c M_q^s}{\gamma} \tag{2.17}$$

Extrapolation of the linear time dependence in (Eq. 2.14) to the stationary solution in (Eq. 2.17) yields the spectral saturation time t_s of the absorption signal,

$$t_s = \frac{K_q^s}{c\kappa_q} = \frac{M_q^s}{\gamma} \tag{2.18}$$

which determines the maximum effective absorption length,

$$L_{eff} = ct_s = \frac{cM_q^s}{\gamma} \tag{2.19}$$

achievable in the detection of ICA under cw operation. This quantity characterizes the laser dynamics, not the measured absorption line, and is the *fundamental sensitivity limit* [22].

2.4.2 ICAS with Fiber Lasers

ICAS has been successfully used with various types of lasers, however, doped fiber lasers that operate continuously in the visible and infrared spectral ranges are more suitable and convenient for the design of compact and inexpensive gas analyzers for practical field measurements [17]. They require considerably less pump power in the range of some milliwatt which is easily achieved with a diode laser. This combination provides small all-solid-state ICAS sensors for gas detection. Fiber lasers emit a broad spectrum caused by the superposition of homogeneous and inhomogeneous line broadening. This characteristic is an important advantage upon diode lasers because it allows simultaneous measurements in a broad spectral range with no spectral tuning. Moreover, the internal loss in the fiber is relatively small, and the overall cavity loss may be as low as 10% per round trip which results mostly from the efficiency of the optical coupling of the external part of the cavity to the fiber [23].

Intracavity absorption measurements can be easily performed with an Er^{3+}-doped fiber laser (EDFL). At the telecommunications band, Er^{3+} ions are used as the amplifying medium. Tuning range extends from 1.52 μm to 1.62 μm and includes strong absorption of many atmospheric and combustion relevant molecules such as CO, CO_2, OH, HCN, C_2H_2, H_2S, NH_3, CH_4, H_2O and HI and it is almost free from strong water vapor absorption lines, typical for other lasers [17][24]. EDFL source usually exhibits nearly constant output power across a wide tuning range, high signal-to-noise ratio, excellent power stability, and high tuning speed for fast modulation and detection [25]. The broad gain bandwidths of the fiber gain mediums, such as EDFL, cover the absorption lines of a number of pollutant gases and thus permit multi-gas detection without need to use individual lasers with wavelengths designed specifically for the absorption lines of different gases [26]. Several experimental systems with EDFL have been built for absorption measurements using a "single-mode" regime of intracavity laser [26][27]. However, as it is expected [22], the sensitivity enhancement factor carried out with these systems is less than 100 ($L_{eff} < 10$ m).

The fundamental sensitivity limit depends on a number of factors which are affected by the optical components and the fiber cavity design [28]. For instance, the limit is expected to increase with the pump rate, however experiments show that the sensitivity of many lasers does not comply this prediction. Only diode lasers have proven to conform this prediction. Experiments carried out with Nd^{3+} and Yb^{3+} fiber lasers have confirmed that Rayleigh scattering is the limiting factor of these systems [29].

2.4.3 Perturbation of ICAS Sensitivity

The maximum sensitivity of multimode lasers to ICA is limited by different kind of perturbation of the laser dynamics. Three types of perturbations are considered, whose effects depend in qualitatively different ways on the strength of the intracavity light. The respective dominance is schematically indicated in Fig. 2.5.

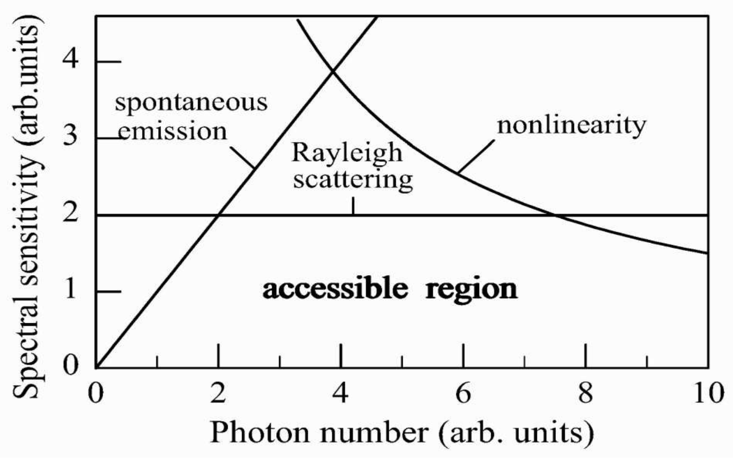

Figure 2. 5 Limitation of ICAS sensitivity

The spontaneous emission is fundamental and present in all lasers. In the specific case of diode lasers it has been proven to be the dominant perturbation. Their sensitivity increases with the pump rate however it is poorer than that of other laser types. The dominance of spontaneous emission is brought about by their high internal loss. Other lasers show far lower loss, and therefore, a higher fundamental sensitivity limit.

Rayleigh scattering of the laser light off local fluctuations of density and temperature in a dense gain material shifts the frequency and the phase of a fraction of the light in the cavity modes. Since the frequency shift is small, the scattered light remains in the same mode and disturbs the phase coherence of the light [30]. Whenever Rayleigh scattering is assumed to be the dominant perturbation, the sensitivity of ICA is not expected to vary with the photon numbers in laser modes. Such effect is known to be the dominant perturbation in solid-state lasers, e.g., fiber lasers. A short gain medium can therefore reduce the effect, such as Ti: Sapphire laser which fills a smaller fraction of the cavity length, once compared with a fiber laser [22].

The most important nonlinearities perturbing the laser dynamics of fiber lasers and reducing their sensitivity to ICAS are spatial inhomogeneity (hole burning) and stimulated Brillouim scattering (SBS) in the gain medium [23]. Spatial inhomogeneity provides strong mode coupling in fiber lasers. It results in antiphase cross-saturation dynamics of the transient modal emission featuring low frequency relaxation oscillations.

SBS corresponds to interactions between optical signals and acoustic waves within the fiber. It can be described as a classical three-wave interaction involving the incident (pump) wave, an acoustic wave and a Stokes wave. The pump wave generates an acoustic wave through electrostriction, which in turn causes a periodic modulation of the refractive index, creating a Bragg grating. This induced grating which propagates with a velocity V_a will be responsible of dispersing the pump signal through a Bragg diffraction. Due to the Doppler effect the dispersed radiation has a lower frequency than the pump signal and the opposite direction [31][32].

3 Experimental Setup and Laser Characterization

The fiber used in the experimental setup is silicate fiber doped with Er^{3+} and germanium (GeO_2) within its core. We use a single mode fiber (Liekki/nLight Er16-8/125) with a numerical aperture N.A. = 0.13, cut off wavelength 1100 nm – 1400 nm, core diameter d = 8 µm. Attenuation at 1530 nm is 16 dB/m. Both ends of the fiber are cleaved perpendicular to the optical axis with a (York FK12 fiber cleaver). For the linear cavity setup, a mirror for the laser wavelength was placed onto one fiber end of the fiber. The second end was anti-reflective coated in order to avoid interference due to back-reflected light.

3.1 Fiber Preparation

Firstly, the fibers used in this preparation were inserted into a suitable fitting to be easily introduced into the laser system. Glass capillaries were utilized for that purpose. Its internal diameter is only slightly larger than the outside diameter of the fibers.

3.1.1 Glass capillary

After the fibers were cut to its desired length, the coating was removed at the fiber ends. The process is followed by gluing the fiber ends into the glass capillary. For this purpose, the fiber end was inserted through the glass capillary such that a small part is left outside.

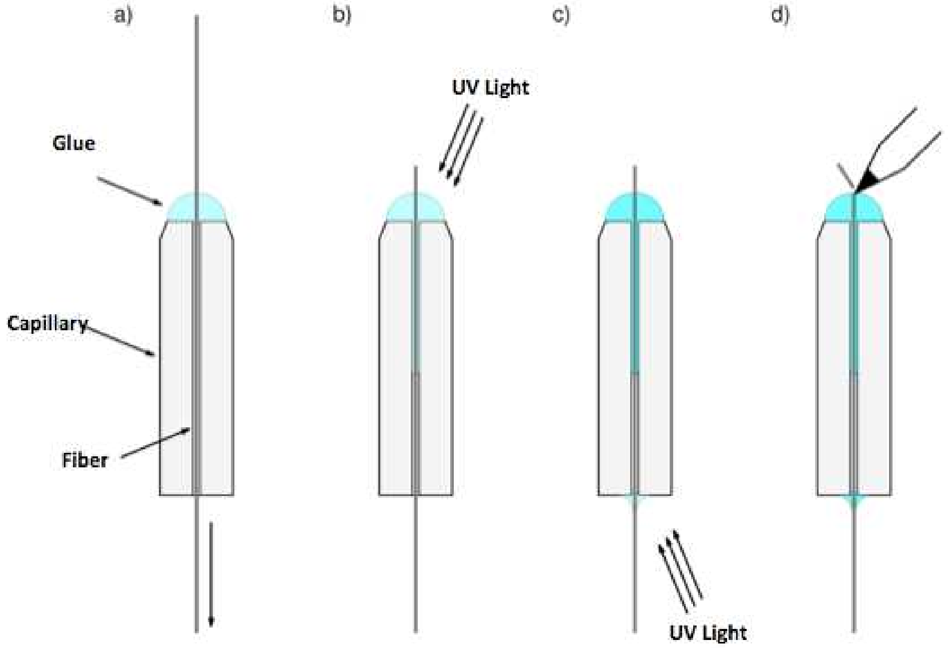

Figure 3.1 Schematic illustration of the insertion and gluing a fiber into a glass capillary

Hereafter liquid adhesive is dropped onto the capillary’s surface in such way that the fiber is completely immersed in the liquid adhesive, in the meantime the fiber is pulled slowly in order to fill up the space with adhesive between the fiber and capillary (Fig. 3.1a). To harden the adhesive, UV light is irradiated and after some seconds the adhesive turns solidified (Fig. 3.1b). A smaller amount of adhesive is then placed on the other side of the capillary followed by curing (Fig. 3.1c). At last, the remain piece of the fiber may be cut away (Fig. 3.1d).

3.1.2 Polishing

The next step consists of polishing the fiber end with four polishing films of different grain size. An aluminum oxide film of 12 µm grain size was used to ablate the adhesive drops into a plane surface. Afterwards a 5 µm followed by a 3 µm silicon film was used to fine smooth the surface obtained before. To conclude the polishing, a 1 µm aluminum oxide film was used to remove even the smallest scratches. Polishing time was about 5 to 10 seconds each round. Both the polishing table and polishing films were properly cleaned with alcohol before each round. During the polishing process, after each round, the result was verified under an electronic microscope in order to control the most convenient polishing time. At the end, there should be no scratches or debris in the vicinity of the fiber core. The fiber-polishing machine used in this process is (Ultratech 8801-1).

3.1.3 Dielectric mirror

After the polishing process is complete, a dielectric mirror must be glued directly onto the polished fiber’s end surface. It will act as the input side of the fiber laser and therefore, a perfect fitting is desirable. The dielectric mirror consists of a sequence of thin layers of different refractive indices. This sequence will enable the pump light to pass through while reflecting the laser light. The mirror about four square millimeters size is placed onto the polished surface and illuminated with monochromatic light. When the distance from the fiber’s end surface to the mirror is smaller than the coherence length of the light, it creates the so-called Newton rings. The mirror is pressed with a slide slightly against the surface and then the fiber is oriented related to the mirror so that the ring system extends concentrically around the fiber cladding and the center light extinction takes place. If there is no new ring in the center, then the alignment is optimal. This alignment is performed under a microscope with 50 times magnification. Blue light from an LED proved to be suitable. Hereafter a drop of liquid adhesive is inserted around each mirror’s edge and then cured with UV light.

3.1.4 Antireflective coating

In order to realize an antireflective coating, the fiber must experience the same procedure as with the glass capillary. Hereafter the fiber was placed into the coating machine (self-made) for coating by vapor deposition. The machine works with Magnesium Fluoride (MgF_2) and Zinc Sulfide (ZnS). The layer sequence is shown in Table 1.

Layer	Material	Physical thickness (nm)
1	MgF_2	72
2	ZnS	42
3	MgF_2	377

Table 1 Sequence of layers of the antireflective coating

Using a reference glass, which was placed along with the fibers in the coating machine, the layer progress was controlled. Its transmission curve reference was measured on a spectrophotometer (Varian Cary 5000 UV-Vis-NIR). The measured data contains information about the transmission of the reference plate. The deposition of the layers is done alternately; the first and the last layer must always consist of Magnesium Fluoride. This is due to the better adhesion to the glass and greater resistance to air. The control of layer thickness takes place during the vapor deposition process of optical reference glasses. This is accomplished by irradiating the reference glass with a monochromatic light and by recording the reflected light with a photodiode. The reflectance signal is recorded on a *xy* recorder. It provides clear information about the current thickness of the layer. The start and the end of the evaporation step can be initiated manually with a shutter valve.

3.2 Experimental Setup

After the fibers were prepared, the fiber laser can be built. Initially all the components and adjustments used on the setup will be briefly described.

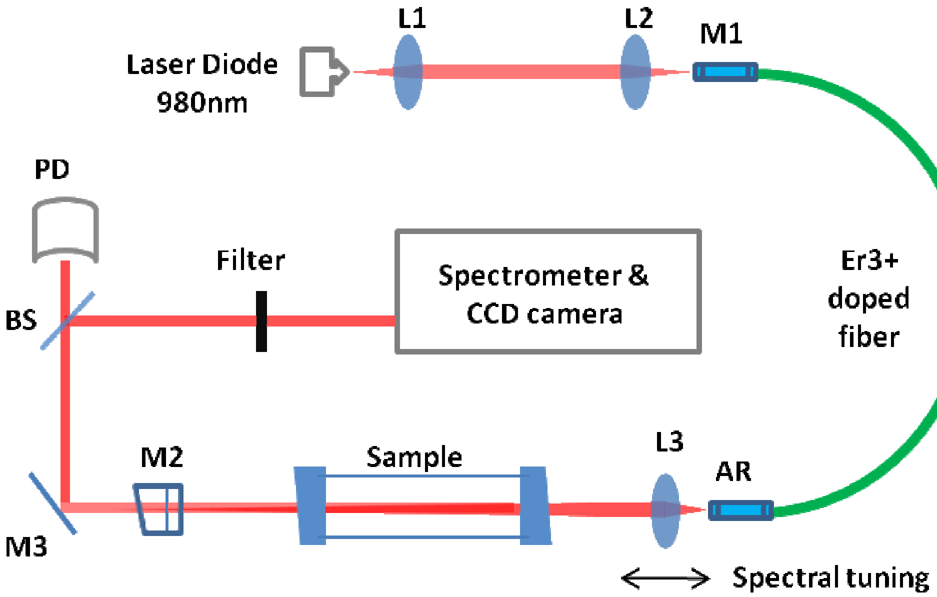

Figure 3. 2 Experimental setup of intracavity absorption measurements with a fiber laser with a linear cavity configuration

Fig. 3.2 shows a schematic setup of the fiber laser with all components. A laser diode at wavelength 980 nm is used as pump source (Axcel Photonics, M9-980-0300-S50). The laser diode is driven by a laser diode controller (Thorlabs, LDC 210 C) with a current in the range of 0 – 400 mA. Right in front of the laser diode stands a collimating aspheric lens L1 (Thorlabs, N.A. = 0.55, f = 4.5 mm) which is anti-reflective coated from 600 nm to 1050 nm (R < 0.5%). Back reflections into the laser diode may cause fluctuations of the output power or even damage the laser diode. The pump light is focused by an aspheric lens L2 (Thorlabs, N.A. = 0.25, f = 11 mm) into the fiber. The mirror M1 reflects the laser wavelength 1550 nm but is anti-reflective for the pump wavelength 980 nm. The focused beam must fall exactly on the micron-scale core of the fiber in order to be coupled into the fiber. For this purpose, the lens L2 is mounted on *X*-*Y*-*Z* translation stage with 50 nm accuracy of positioning (Thorlabs, AMA007/M). Therefore the distance and the relative positions of the lens and fiber end are perfectly adjustable. The fiber capillary where it holds the fiber end is mounted into an aluminum cylinder which is fitted in a holder with the same area as the moving table (translation stage). At the other end of the fiber, the emitted light is collected with a collimating aspheric lens L3 (Thorlabs, N.A. = 0.3, f = 15 mm) and focused on the output mirror M2. The lens L3 is anti-reflective coated at 1.5 to 2 µm and mounted on a second *X*-*Y*-*Z* translation stage. The laser emission spectrum can be tuned by moving lens L3 along the optical axis, using the effect of chromatic aberration. The output mirror M2 has a transmission at the laser wavelength of about 1%. It is mounted into a mirror holder that can be tilted vertically and horizontally. A broadband filter (Thorlabs, FEL1100) is introduced into the system in order to eliminate pump radiation behind the output mirror. Its cut off wavelength is about 1100 nm. The emerging laser light is then reflected by the mirror M3 to a 95:5 beam splitter which splits 5 % of the laser light into a photodiode and 95 % to the spectrometer. In the open part of the resonator between the lens and the output mirror, an absorption cell can be placed, enabling specific gases to be investigated. The spectrum of the laser radiation is analyzed by a high resolution grating spectrometer with a 300 grooves/mm grating operating in the 2nd or 4th order. The spectra are recorded by an IR linear CCD camera (1024 pixels of 25 µm, Sensors unlimited SU1024LDV-1.7RT) and stored by a computer. The total spectral resolution of the recording system in the 4th order of diffraction is 0.12 cm^{-1}.

3.2.1 Laser adjustment

The adjustment of the laser consists in coupling the pump light into the fiber followed by alignment of mirror M2 and Lens L3, so that the laser operation is achieved. The lowest laser threshold is desirable because it corresponds to low cavity losses and therefore leads to higher achievable sensitivity. The beam profile during the adjustment can be observed by using a fluorescent card.

Coupling into the fiber

First step of adjusting is coupling the light into the fiber. In the beginning, the fiber end should be located slightly closer than the focal point of the lens. The power meter (LM-2-Vis, Coherent) is located behind the lens L2 to measure the emerging power. The laser diode current is set to 80 mA at the beginning of the adjustment. The emerging power will be increased by adjusting the position of the fiber perpendicular to the beam path. After that, the fiber is moved along the beam such that a reduced beam waist is encountered and thus the emerging power will increase due to higher power being focused into the fiber core. If the overlap of the light spot with the core is too small, that means that the core is not fully taken. As a result, the measured power falls down. It is somewhat adjusted back to the maximum output power and again turn the perpendicular position to optimize the optical path. These steps ate repeated until the emerging power cannot be further enhanced.

Back coupling into the fiber

The next step consists of coupling the light back into the fiber by aligning the lens L3 and output mirror. Firstly, the coupling lens is moved so that the light beam in centrally focused on the outcoupling mirror. Now, the outcoupling mirror is tilted so that the reflected beam meets back the lens where the incoming beam was localized. Hereafter the coupling lens is moved along the beam direction in order to optimize the focus of the light behind the outcoupling mirror where the pump light is refrained by a broadband filter. Behind the filter, another power meter (LM-2-IR, Coherent) is placed in order to further improve the measured signal of the laser output power.

3.3 Laser Characterization

The first step for laser characterization consists in measuring the diode laser efficiency curve and the fiber laser efficiency curve. For this purpose, the power meter is placed in front of the laser diode or behind the fiber laser and filter. The performance of the laser diode is shown in Fig. 3.3 as a function of the laser diode current. The diode laser power above the threshold exhibits a linear response.

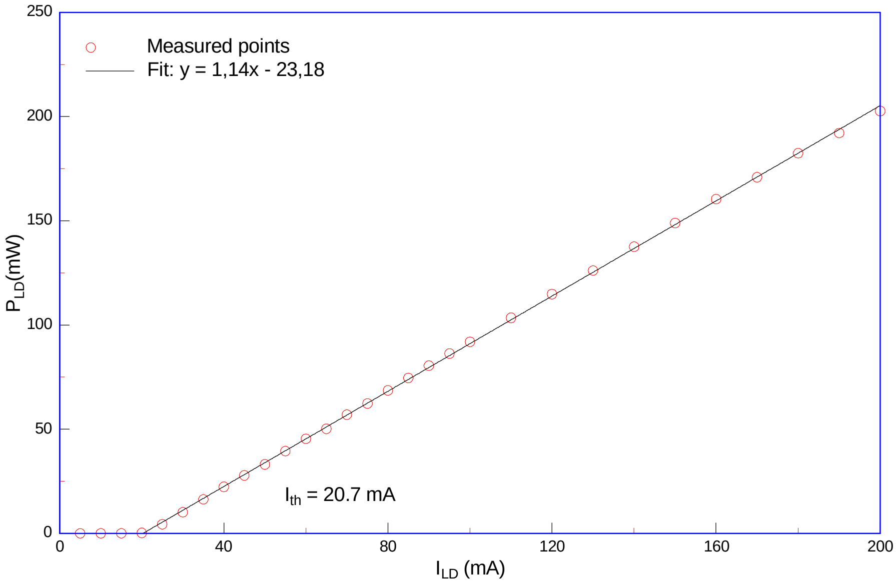

Figure 3. 3 Output pump power vs. current

Fig. 3.4 shows the output power of an Er^{3+}-doped fiber laser as a function of the laser diode power. The laser threshold corresponds to 7.5 mW and with a maximum output power at 0.6 mW which is enough for the spectral recording.

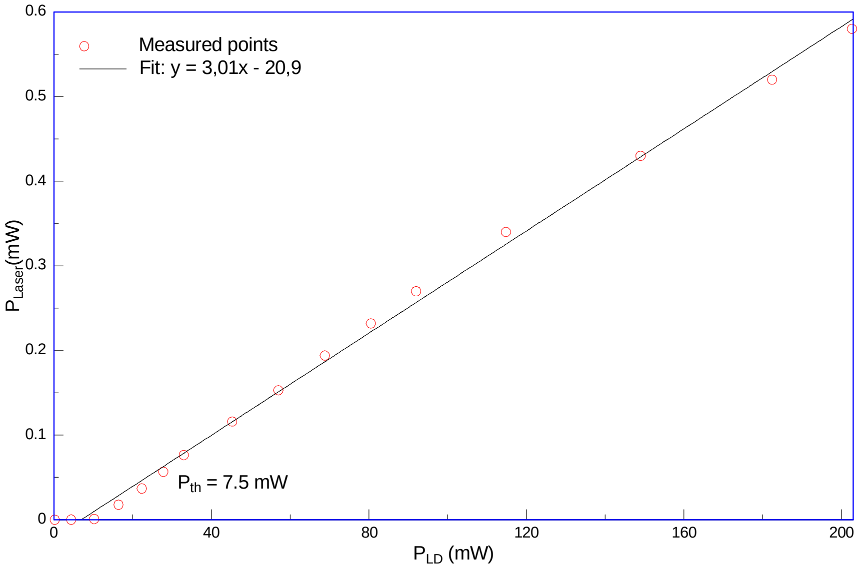

Figure 3. 4 Output power of the Er^{3+}-doped fiber laser vs. pump power

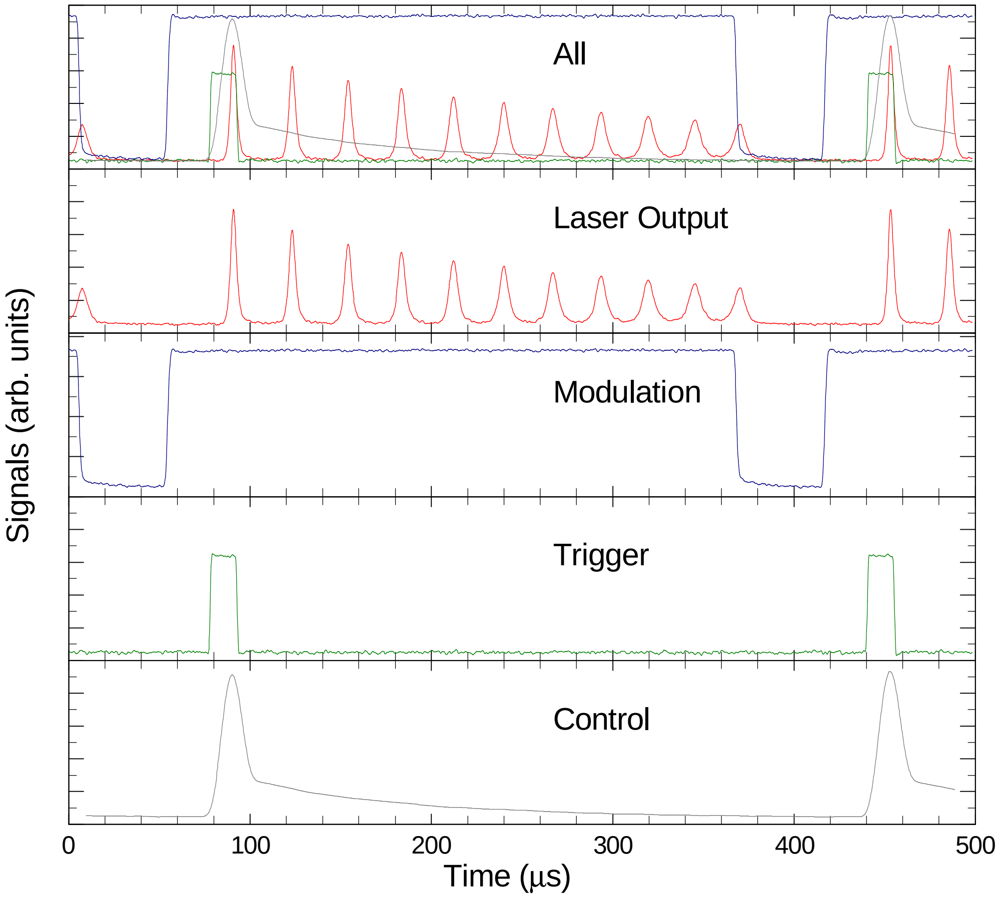

Figure 3. 5 Representation of the signals for the measurement of laser emission spectra during selected time intervals

Fig. 3.5 shows the switching cycle for data acquisition. The sensitivity was set by the controlled step modulation of the pump power above and below the threshold (blue). After switching the pump laser above the threshold, the fiber laser starts with the emission showing strong relaxation oscillations (red) as is typical with solid-state lasers [24]. The duration of the first relaxation peaks of the laser emission is shorter than peak separations. The integration time of the diode array spectrograph can be activated by using a trigger signal (green). This makes it possible to record emission spectra of the fiber laser during a defined time window. The diode array provides a control signal (gray) back, indicating the time window of measurement. The period of modulation was selected so, that after the first relaxation peak the pump power drops below threshold. In this way only one relaxation peak appears in the laser emission and the sensitivity is determined by the time t of the appearance of the maximum laser power in respect to the onset of laser oscillations. This time was selected to be 20 µs by controlling the pump power. The resulting effective path length is $L_{eff} = ct$ = 6 km (Eq. 3.1). In case that the absorber does not occupy the complete cavity, the filling factor of the cavity must be taken into account.

Fig. 3.6 shows the emission spectrum of a 2 m long Er^{3+}-doped fiber laser under cw operation recorded at different positions of intracavity lens. The tuning range extends from 6540 cm^{-1} to 6235 cm^{-1} (1.53 µm – 1.60 µm). The tuning of the laser wavelength is performed by shifting the position of the lens L3 in the resonator. Because of the dispersion of the lens material, the focal length of the lens depends on the wavelength of light. Depending on the position of the lens along the optical axis, a specific wavelength range is optimally focused on the output mirror M2 and fed back into the fiber. Larger or smaller wavelengths of light undergoes greater circulation losses, whereby the net gain is moved so that the emission wavelength of the laser in the direction of the best back-coupling wavelength. The strength of this shift depends not only on the dispersion of the lens material also on the gain profile of the active medium. For a general purpose of a laser system for intracavity absorption spectroscopy, the largest possible tunability is desirable.

Fig. 3.7 shows the emission spectrum of a 2 m long Er^{3+}-doped fiber laser recorded during the first pulse of relaxation oscillation. The tuning range extends from 6540 cm^{-1} to 6220 cm^{-1} (1.53 µm – 1.61 µm). An absorption cell of 12 cm length with no windows is placed in the resonator. A constant flow of CO_2 is introduced into the absorption cell. As a result, it is possible to identify the regions where strong CO_2 absorption lines take place as it is essential for the aim of this research. Spectral calibration of these absorption lines is achieved by comparing the ICA spectra to a transmission spectrum of CO_2 absorption calculated from the HITRAN database [33].

Sensitivity of intracavity laser spectroscopy with a cw laser is determined by the spectral saturation time t_s [22] which depends upon laser parameters. However, if the duration of the laser oscillations is selected to be $t \ll t_s$, the absorption path length acquires a very defined value

$$L_{eff} = ct \tag{3.1}$$

It allows precise measurements of absorption coefficients and molecular concentrations.

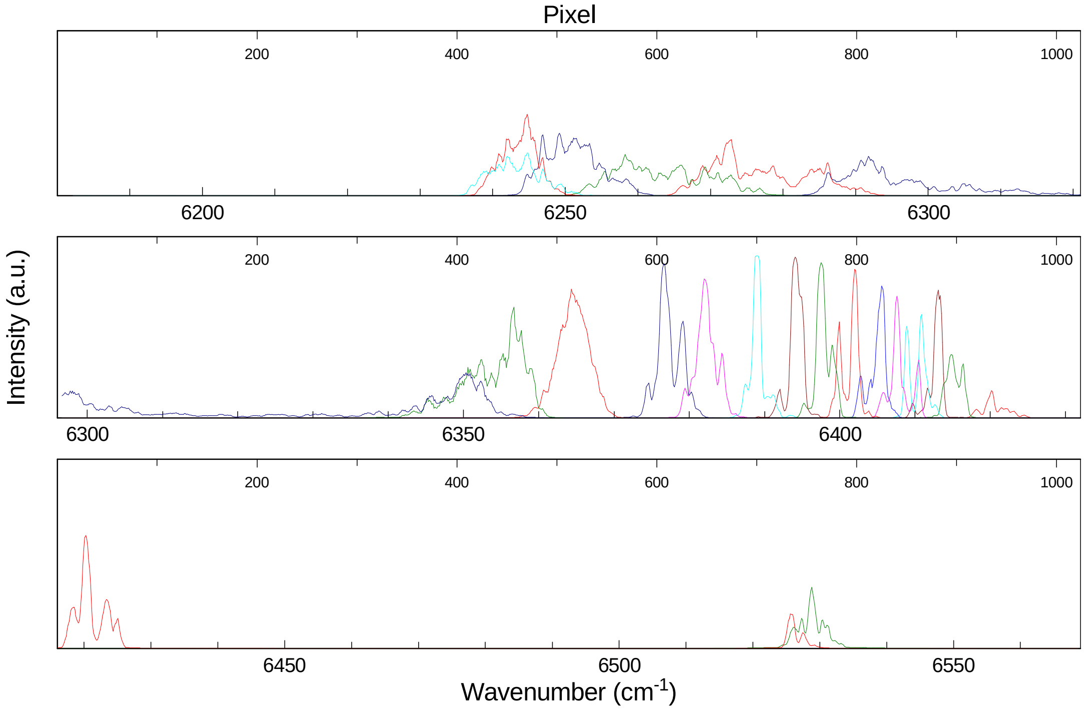

Figure 3.6 Emission spectra of a cw Er^{3+}-doped fiber laser at different positions of the intracavity lens L3. Individual emission spectra are shown with different colors

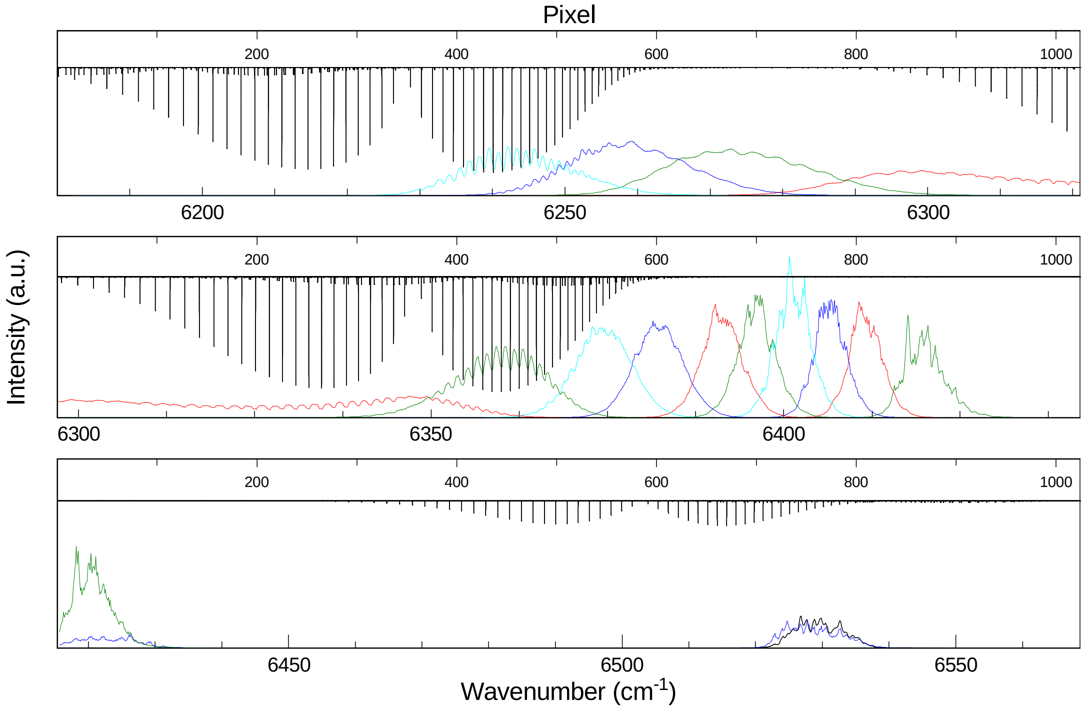

Figure 3.7 Emission spectra of the first relaxation peak of an Er^{3+}-doped fiber laser at different positions of the intracavity lens L3 including intracavity CO_2 absorption (black). Individual emission spectra are shown with different colors

The recording and evaluating of intracavity absorption spectra of CO_2 is demonstrated in Fig. 3.8. The bottom record shows the emission spectrum of the Er^{3+}-doped fiber laser with a 2 m long fiber at one selected position of the intracavity lens for an open cavity. This spectrum exhibits a background structure due to etalon fringes caused by reflection from various optical components in the laser cavity and from possible imperfections in the fiber. This structure is well reproduced in all spectra including the spectrum with CO_2 at atmospheric pressure in the absorption cell, presented in the middle record. This background structure can be eliminated by dividing the spectrum with intracavity absorber (middle diagram) by the spectrum without absorber (bottom diagram). The spectrum in the top diagram shows the normalized spectrum obtained in this way.

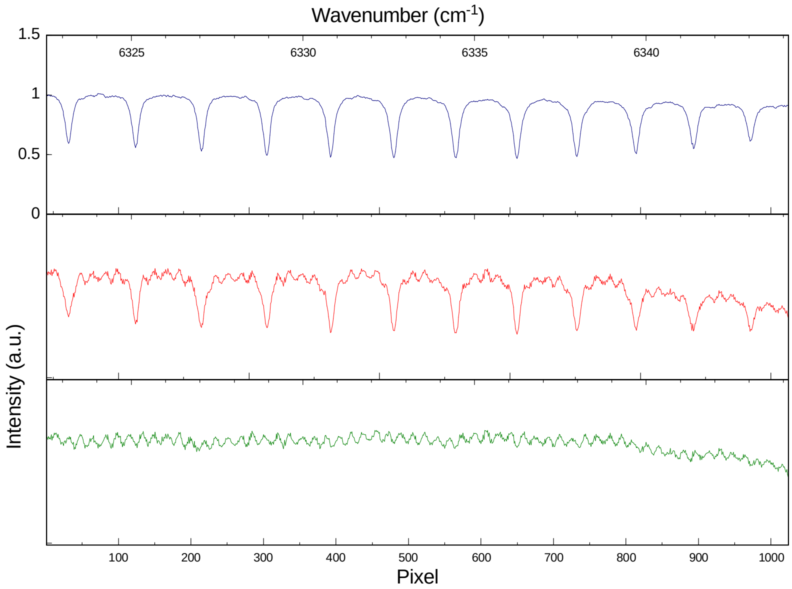

Figure 3. 8 Emission spectrum of an Er^{3+} doped fiber laser without intracavity absorption (green), with intracavity absorption of CO2 (red), and normalized spectrum of intracavity absorption (blue)

4 Absorption Measurements

Breath analysis is one of the several applications that can be efficiently performed with ICAS. It is a promising field of medicine and medical instrumentation. The next section will present an introduction to human breath with a brief comparison of some spectroscopic techniques applied to this purpose.

4.1 Human Breath

To date, researchers have identified over 1000 different compounds contained in human breath. These molecules have both endogenous and exogenous origins and provide information about physiological processes occurring in the body as well as environment-related ingestion or absorption of contaminants [34][35]. While the presence and concentration of many of these molecules are poorly understood, many 'biomarker' molecules have been correlated to specific diseases and metabolic processes. Such correlations can result in non-invasive methods of health screening for a wide variety of medical conditions. Several methods of trace molecular detection have been applied to the problem of breath analysis including optical detection [36][37], mass spectrometry [38][39], and electronic noses [40][41].

To understand the choice of optical detection as the preferred technique for breath analysis, we first evaluate the available techniques in the context of the system criteria. For instance, mass spectrometry (MS) is extremely sensitive and thus capable of detecting very small quantities of the analyte molecule. However, when several molecules are present, MS has difficulty identifying a single component of the mixture. To remedy this problem, MS is often used in conjunction with gas chromatography to separate out various components of a mixture prior to measurement. While these hybrid systems are highly sensitive and accurate for a large number of biomarkers, they are also large, complex, expensive, and require a long period of time to perform a measurement [41]. Conversely, electronic nose devices are typically inexpensive and perform measurements rapidly. However, these devices, which are designed to measure volatile organic compounds, have difficulty distinguishing and accurately measuring concentrations of individual molecules from the group they are designed to detect [42]. Optical detection provides a good compromise as a general approach that can be applied to many molecules.

The unique absorption spectrum of each molecule allows accurate identification and concentration measurements of a single molecule in the presence of many others. While systems have already been using tunable laser diodes [43][44] and cavity ring down - tested methods for breath analysis [45], they proved to be fruitful for a variety of reasons but still not as mature. A system with Er^{3+}-ICAS is therefore very promising, as it provides the possibility of time resolved online measurements combined with a very high spectral sensitivity. Online methods are characterized by real-time gas sampling and analysis. The resulting concentration along with other variables such as flow rate are continuously captured without significant delay whilst offline methods generally require time-consuming sample preconcentration [46].

In the 1.52 µm to 1.62 µm spectral region, there are a few biomarkers that exist in human breath in detectable quantities. The measurements presented in this research explore one of these biomarkers: CO_2.

The aim of our breath measurements involves the analysis of stable isotopes. Exhaled CO_2 is of a medical interest e.g., the ratio of $^{13}CO_2$ to $^{12}CO_2$ can be used to determine if a patient is infected with *Heliobacter pylori*, a common cause of ulcers.

The exhaled gas is not homogeneous. For a health individual, the first part of a breath consists in “dead-space” air from the upper airway, where there is no air exchange between the blood and breath air. The following part of the breath is “alveolar” breath, which comes from lungs where gaseous exchange between the blood and breath air take place [34].

4.2 Calibration

The estimation of the sample concentration from intracavity absorption spectra can be achieved by the calibration of the absorption signal. Such a calibration can be performed in the experiment or calculated form the HITRAN database.

The determination of a proper flow for calibration of CO_2 was first performed. The gas flows were adjusted by calibrated mass-flow controllers (1179, MKS instruments) operated by a two-channel control unit (MKS Instruments PR4000). Ten different total flows (5 % CO_2 and 95 % N_2) given in sccm (standard cubic centimeter per minute) were selected (Fig. 4.1). Nitrogen (N_2) is used as a buffer gas. A gas cylinder containing CO_2 is directly connected to the first mass-flow controller which allows to regulate a constant CO_2 flow up to 77 sccm. The second mass-flow controller is connected to a N_2 gas cylinder and regulates the N_2 flow up to 1000 sccm. Both flows are led to an open absorption cell of 12 cm long.

Fig. 4.2 shows the absorption signal as a function of flow. The absorption signal exhibits saturation at flows above 300 sccm. The flow of 700 sccm has been chosen for absorption measurements. This flow enables the range of CO_2 to vary from 0.14 % to 11 %. The rate of CO_2 present in a normal human exhalation is 4 % to 7 %.

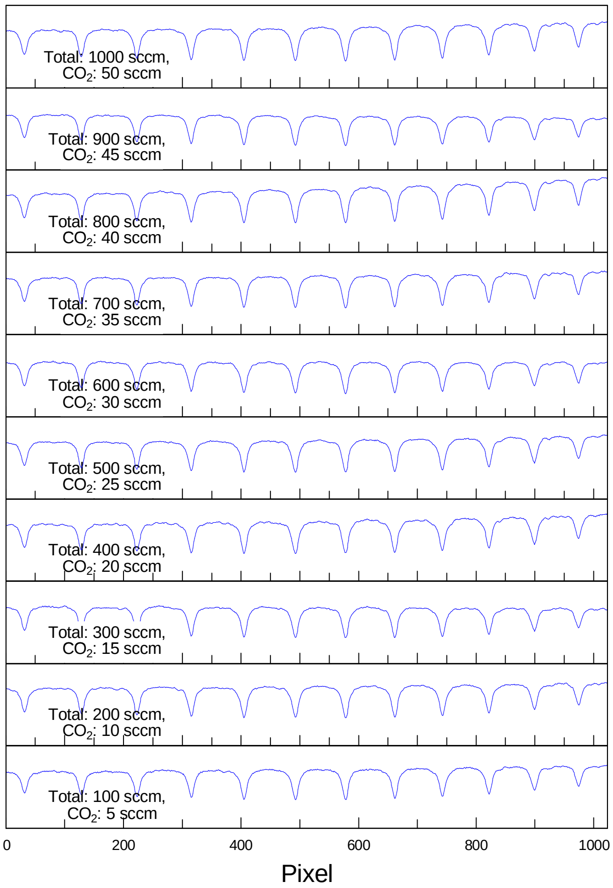

Figure 4.1 Spectra of Er^{3+}-doped fiber laser with ten different flows of CO_2 and N_2 in the cavity

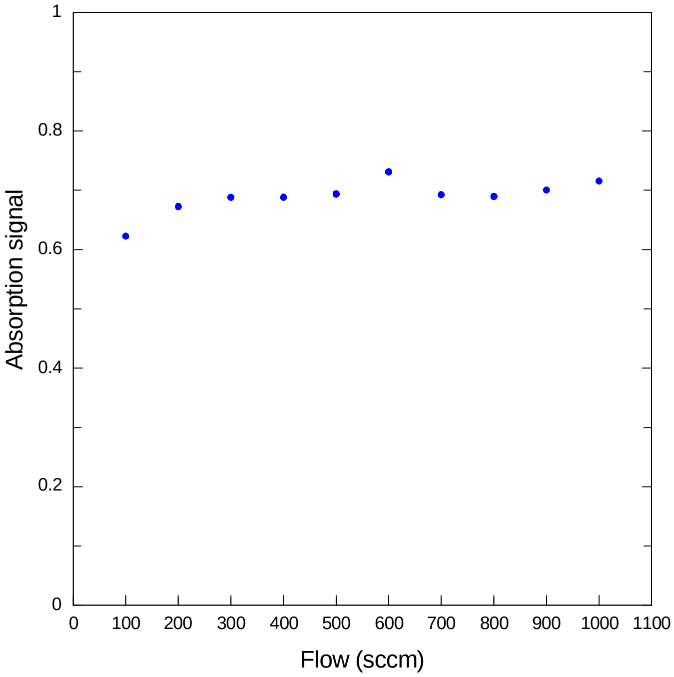

Figure 4. 2 Absorption signal of CO2 absorption lines from Fig. 4.1 as a function of gas flow

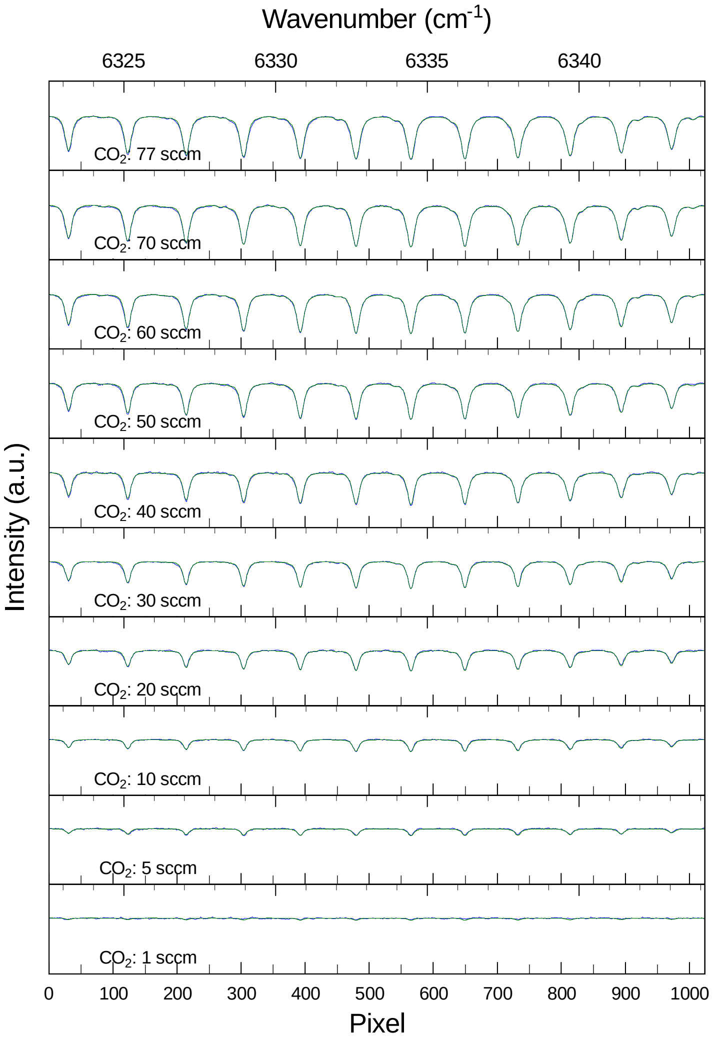

Figure 4. 3 Normalized intracavity absorption spectra of CO_2 recorded with different CO_2 flows (blue). HITRAN spectra (green) are superimposed with the measured spectra

Normalized intracavity absorption spectra of CO_2, recorded with different CO_2 flows varying from 1 sccm to 77 sccm with a total flow of 700 sccm are presented in Fig. 4.3. The spectral calibration can be performed by evaluating the absorption signals of the CO_2 lines for the same absorption lines of CO_2 by HITRAN database. As a result, the HITRAN spectra (green) are superimposed with the measured spectra of CO_2 (blue). In this way, one can observe the high accuracy achieved with ICAS measurements.

Calibration curves in Fig. 4.4 can be used for the estimation of the CO_2 concentration inside the absorption cell. Calibration of these spectra is performed by evaluating the absorption signals at twelve CO_2-lines obtained from fig. 4.3. The absorption signal can be calculated from (Eq. 2.9). Fig.4.4 shows the experimental records calculated from Fig. 4.3 at twelve different CO_2 absorption lines which are indicated by different colors or shapes. Correspondent wavenumbers are also specified. The experimental records correspond to the CO_2 concentration inside the absorption cell plus the CO_2 concentration present in the atmosphere which is about 0.039 %. The line fit is applied to the experimental records in order to enable estimation of CO_2 concentration for an absorption signal ranging up to K =

1.7. Values of CO_2 concentration in the atmosphere can be obtained by the value of concentration at absorption signal, $K = 0$. This leads to a CO_2 concentration of - 0.14 % which corresponds to CO_2 concentration in the air of 0.04 % by taking into account the filling factor of the cavity with an absorber.

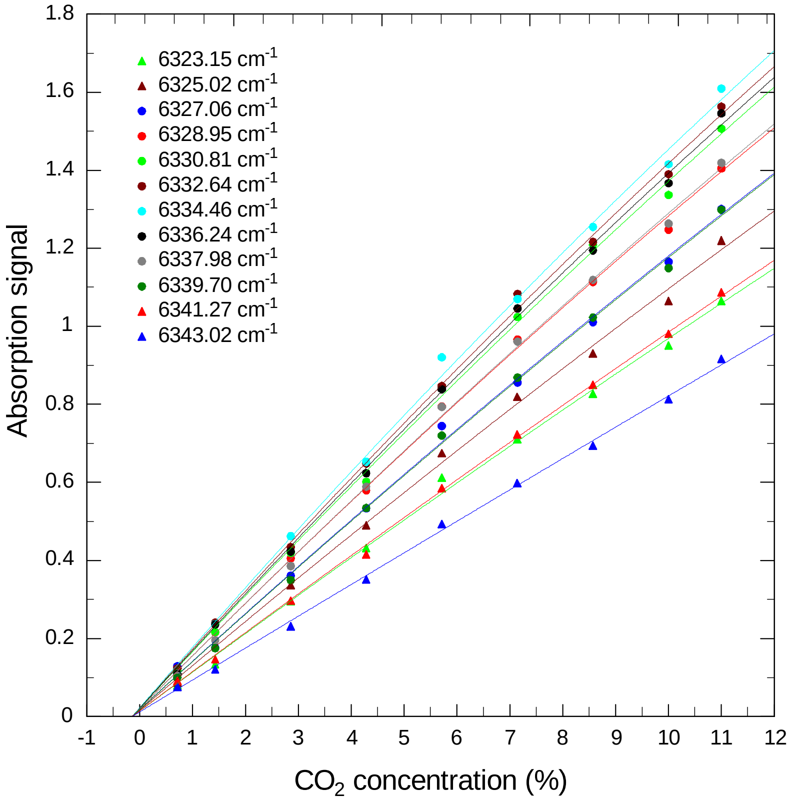

Figure 4.4 Calibration curves used for the estimation of the CO_2 concentration inside the absorption cell.

4.3 Breath Measurements

The procedure we have undertaken to conduct breath measurements was firstly to ensure that the test subject takes a deep breath and then exhales through a mouth piece which is connected via a small hose to the absorption cell. In this step, the test subject was instructed to keep a constant flow. The procedure to conduct breath measurements after smoking was to ensure that the test subject takes a breath in a cigarette followed by a normal exhalation, and then the measurement is initiated with the following breath cycle.
The exhalation was monitored in real time by home-made software that enables acquisition and processing of data including averaging. The software was built using the programming language LabVIEW 7.0 (National Instruments).

Fig. 4.5 shows normalized absorption spectra of exhaled breath before and after smoking at selected time interval. The absorption signal was evaluated for the second spectrum counting from the top at each absorption line. The CO_2 concentration was obtained by using calibration in Fig. 4.4. The absorption signals and correspondent CO_2 concentrations are displayed in Table 2. The mean concentration before smoking equals

n_{CO2} = 5.35 % and after smoking n_{CO2} = 5.02 % contained in one single exhalation. In order to perform an online recording of breath CO_2 the absorption lines at 6330.81 cm^{-1} and 6332.64 cm^{-1} were applied to the CO_2 concentration measurements.

Fig. 4.6 and Fig. 4.7 show the online recording of exhaled CO_2 before and after smoking. The first part of the breath consists of a rapid increase of CO_2 concentration due to the mixing of dead space air with the expired alveolar air. The second part consists of a linear increase of CO_2 concentration originated from the alveoli only.

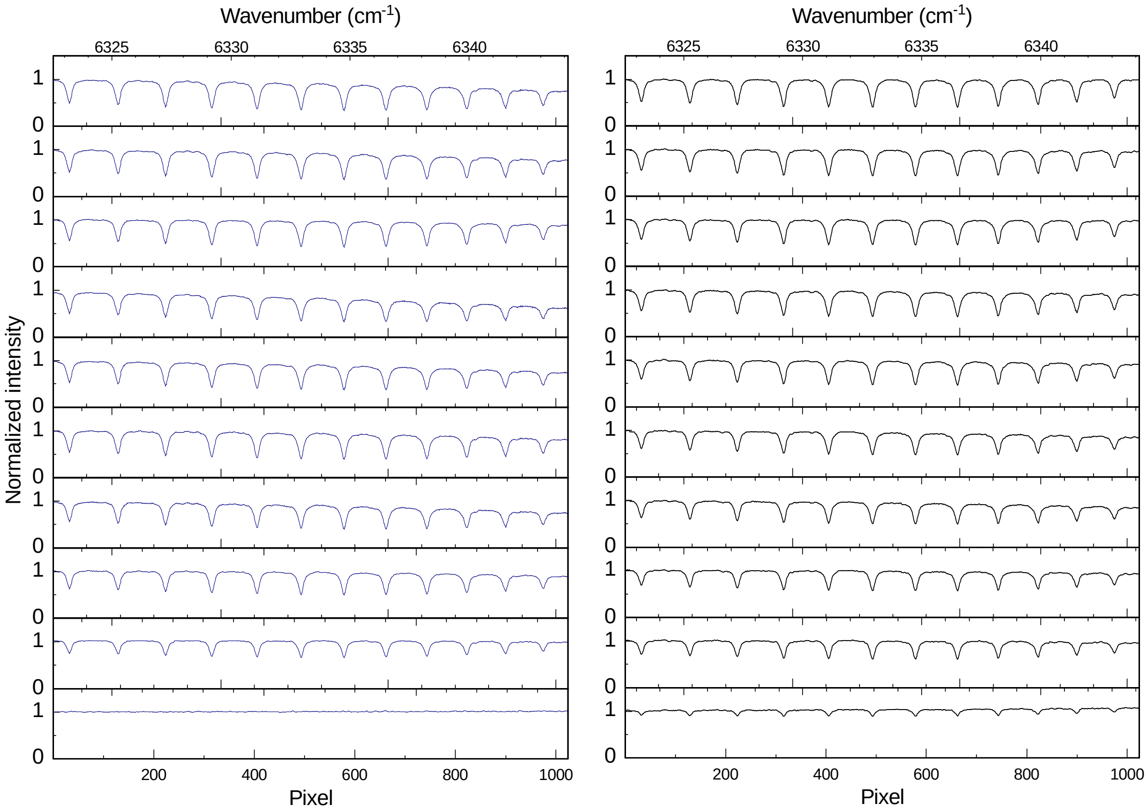

Figure 4.5 Normalized absorption spectra of exhaled breath before (blue) and after (black) smoking. The spectra were recorded at *t* = 1 s (starting at the bottom diagram) to *t* = 10 s

Wavenumber (cm^{-1})	Absorption signal, *K* before / after smoking	CO_2 % before / after smoking
6323.15	0.593 / 0.529	5.96 / 5.26
6325.02	0.609 / 0.590	5.31 / 5.16
6327.06	0.679 / 0.628	5.48 / 5.06
6328.95	0.735 / 0.698	5.45 / 5.16
6330.81	0.769 / 0.733	5.31 / 5.06
6332.64	0.808 / 0.733	5.40 / 4.99
6334.46	0.799 / 0.732	5.19 / 4.72
6336.24	0.784 / 0.732	5.36 / 4.95
6337.98	0.739 / 0.687	5.46 / 5.06
6339.70	0.645 / 0.624	5.21 / 5.04
6341.27	0.578 / 0.538	5.70 / 5.28
6343.02	0.433 / 0.416	5.16 / 4.91

Table 2 Absorption signals and correspondent CO_2 concentration evaluated from Fig. 4.5

Fig. 4.8 shows the online recording of exhaled CO_2 until t = 140 s. In the first part of the exponential decay, from t = 15 s to t = 30 s, CO_2 initiates a rapid decay indicating a relatively quick decrease in CO_2 concentration inside the absorption cell. In the second part, from t = 40 s to t = 120 s, the exponential fit does not match well the experimental record which correspond to a slow decay of CO_2 concentration. This is due to additional CO_2 molecules that remain in the tube used to connect mouthpiece to absorption cell.

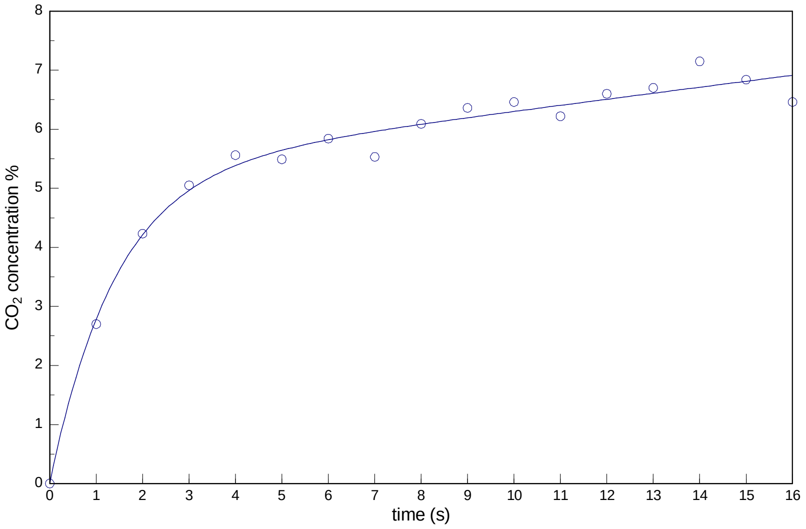

Figure 4.6 Online recording of exhaled CO_2 before smoking. Curve fitting is applied to the experimental records

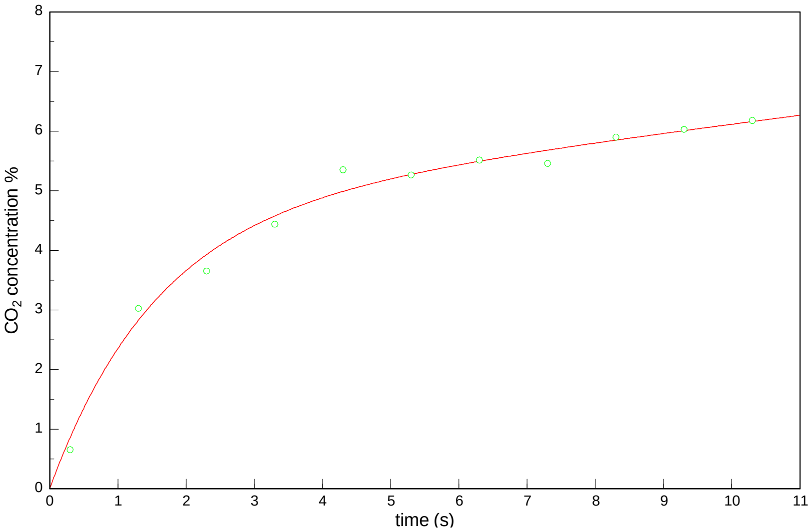

Figure 4.7 Online recording of exhaled CO_2 after smoking. Curve fitting is applied to the experimental records

Fig. 4.9 exhibits a similar behavior compared with Fig. 4.8 however with a shorter time of exhaled breath and correspondent breath decay. For better comparison, mass-flow controllers can be utilized to regulate the exhaled flows to a constant value.

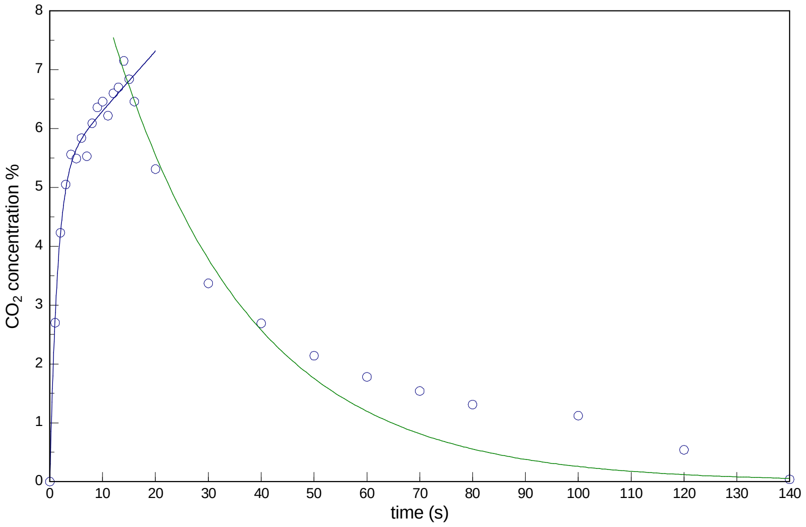

Figure 4.8 Online recording of exhaled CO_2 before smoking until 140 s. Curve fits corresponding to the CO_2 exhalation (blue) and its decrease in the cell (green) are indicated

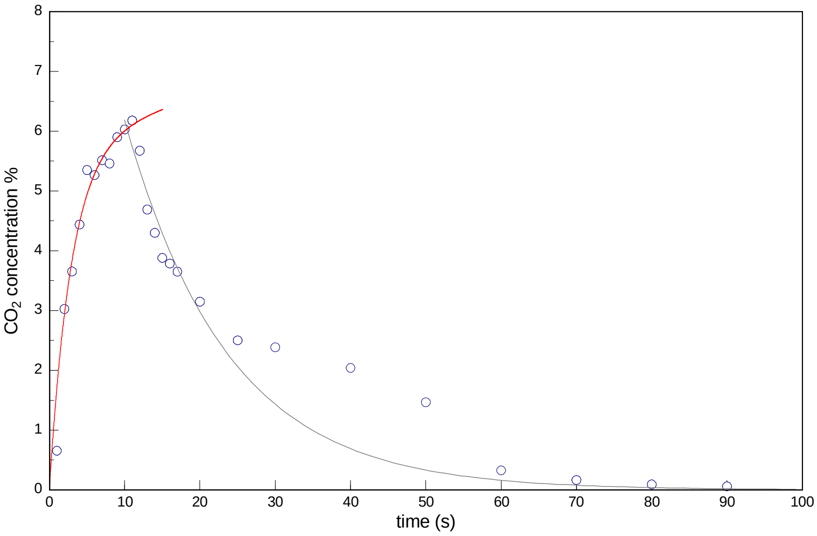

Figure 4.9 Online recording of exhaled CO_2 after smoking until 100 s. Curve fits corresponding to the CO_2 exhalation (red) and its decrease in the cell (grey) are indicated

This experiment performed with ICAS has proven to be a promising technique in the field of medical breath analysis. It is demonstrated to be reliable for time-resolved measurements of CO_2 concentration in exhaled breath. This opens a new gate for further experiments with other gases contained in human breath however in much less concentrations, such as hydrogen cyanide (HCN), acetylene (C_2H_2), Carbon monoxide (CO), Ammonia (NH_3) or ethane (C_2H_6).

In ongoing studies, a gas filling system will be incorporated for low-pressure breath measurements in order to obtain more accuracy and reliability during the measurements. The gas filling system is shown in Fig. 4.10. It consists of two mass-flow controllers operated by a control unit which were already specified to perform the calibration steps. A pressure controller (MKS Instruments 250E) for dynamic mass flows employing a capacity pressure gauge head (MKS Instruments Baratron 221 AHS-D-100) and an electromagnetic valve (MKS Instruments 248A).

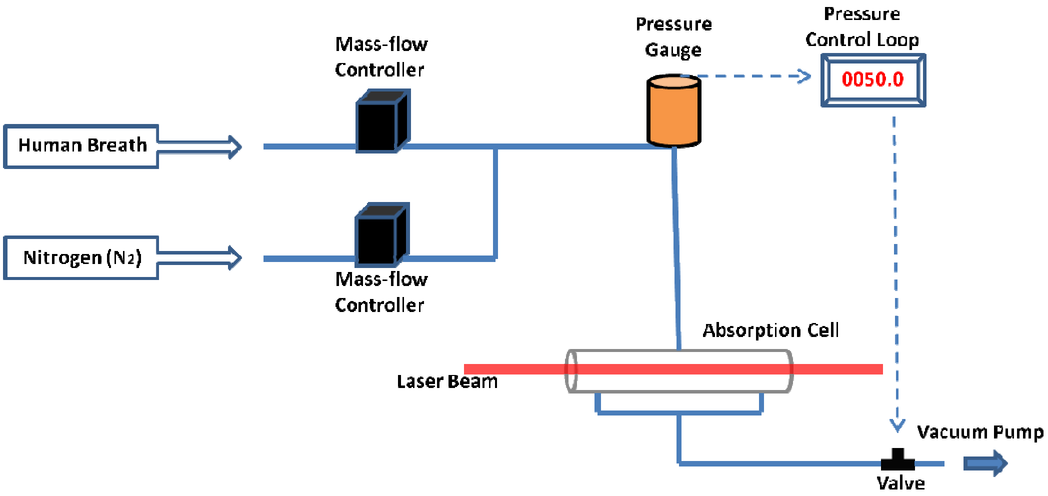

Figure 4.10 Schematic illustration of the gas filling system that can be utilized for future breath measurements performed with ICAS.

For measurements, the absorption cell can be flushed with a gas sample or a certified gas mixture by means of a vacuum pump. The flow rate is adjusted via mass-flow controllers. The pressure inside the absorption cell can be maintained independently of the flow using of a pressure control loop.

4.4 Sensitivity Enhancement

The fiber laser was modified from a linear cavity configuration to a ring configuration in order to enhance the sensitivity of the absorption measurements.

The main phenomena for the limitation of the sensitivity of ICAS using linear fiber lasers are Rayleigh scattering and spatial inhomogeneity of the gain. With the construction of a ring laser one could completely eliminate the spatial inhomogeneity of the gain, because in a ring resonator, there are no longer standing waves. This structure provides a compact solution for realizing a high sensitivity, because it results in weaker etalon structures, since the light propagation takes place only in one direction. By employing a ring cavity, both the parasitic fringes and nonlinear processes can be eliminated. The experimental ring cavity setup is presented in Fig 4.11.

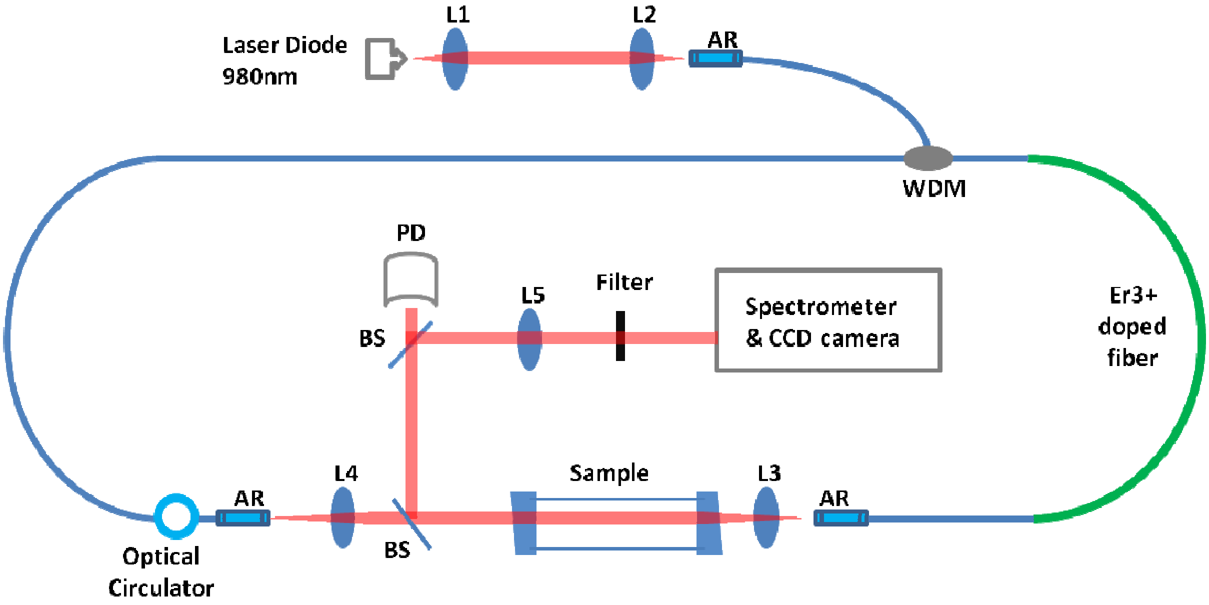

Figure 4.11 Experimental setup of intracavity absorption measurements with a fiber laser with a ring cavity configuration

The conversion from a linear to a ring cavity consisted mainly in the installation of two new optical components, a WDM and an optical circulator. The pump light is coupled into the fiber which is connected to one output of the WDM (Thorlabs, WD202A-FC). Its duty consists in coupling the pump power at 980 nm into the resonator while keeping the laser light at 1550 nm undisturbed. The second WDM output was spliced to the Er^{3+}-fiber and the third output is spliced with a passive piece of fiber connected to an optical circulator (Thorlabs three port circulator 6015-3) which ensures unidirectional operation. The losses in the resonator have however increased and the laser could not be tuned so extensively compared with the linear cavity. The laser threshold is about $P_{th} = 14$ mW.

Fig. 4.12 presents the emission spectrum of a 4 m long Er^{3+}-doped fiber laser recorded during the first pulse of relaxation oscillation. The tuning range extends from 6540 cm^{-1} to 6270 cm^{-1} (1.53 μm – 1.59 μm). An absorption cell of 20 cm length is placed in the open part of the resonator. It is connected to a vacuum pump and to a CO (carbon monoxide) gas cylinder. In this way, a constant pressure of CO can be regulated and introduced into the absorption cell. As a result, it is possible to identify the regions where strong CO absorption lines take place. Spectral calibration of these absorption lines can be achieved by comparing the ICA spectra to a transmission spectrum of CO absorption calculated from the HITRAN database.

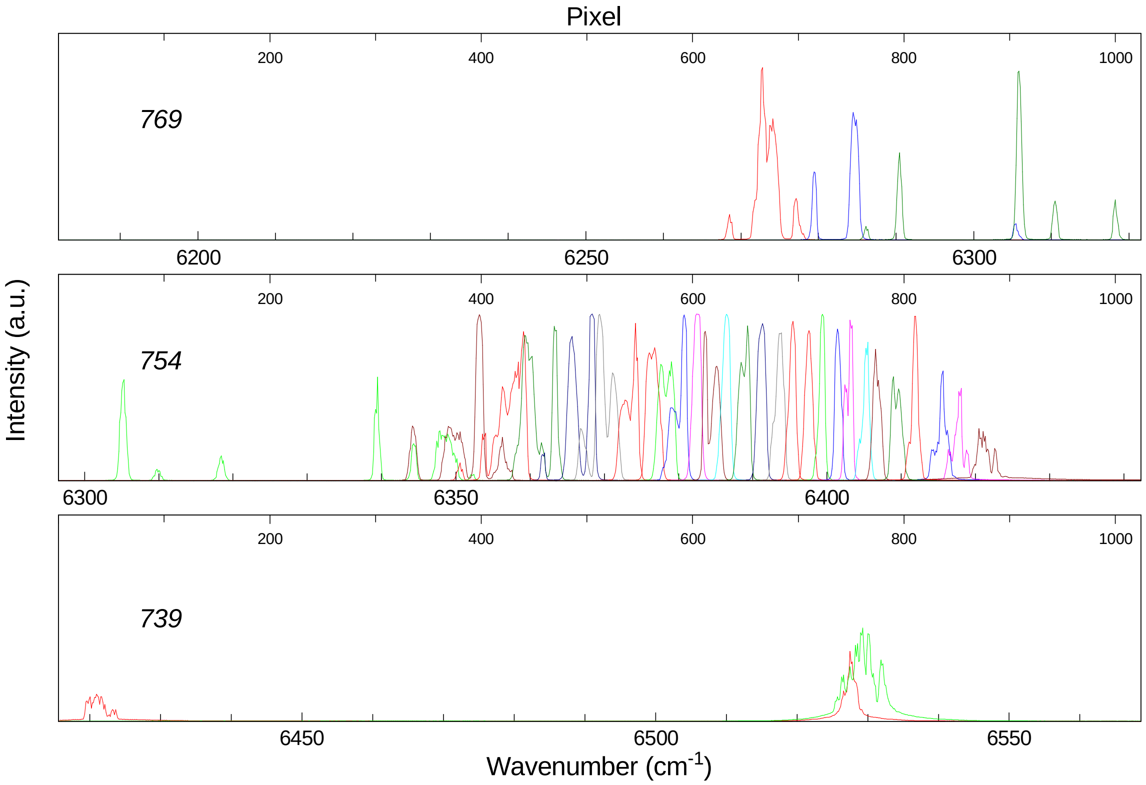

Figure 4.12 Emission spectrum of the first relaxation peak of an Er^{3+}-doped fiber ring laser at different positions of the intracavity lens L3. Individual spectra are shown with different colors

A demonstration of the sensitivity of ICAS measurements with a ring laser configuration is performed with absorption spectra of CO. CO is an important component present in human breath, combustion processes, and atmosphere and therefore its precise monitoring of its concentration is investigated in this configuration.

The recording and evaluating of time resolved intracavity absorption spectra of CO is demonstrated in Fig. 4.13. The records show the time evolution of laser emission with intracavity absorption. These are emission spectra of the laser with CO absorption in the resonator recorded at fourteen different relaxation pulses of laser emission. The time *t* was measured since the beginning of the laser oscillation, and t = 0 can be extrapolated from the plot of the absorption signal versus time, as demonstrated in Fig. 4.14. The time zero is set to be the first pulse, and the interval following the pulse is read from one of the Fig. 4.13 the representation of the laser intensity.

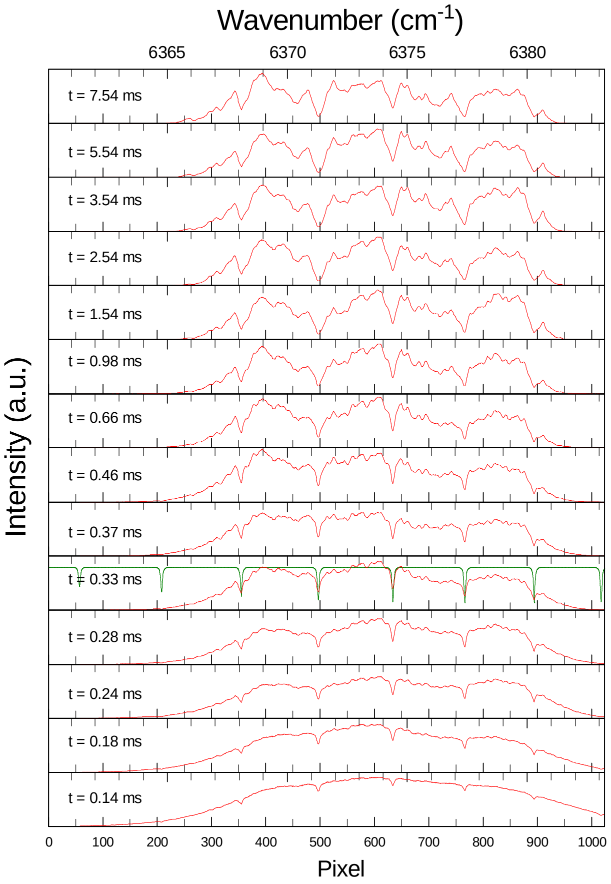

Figure 4.13 Time evolution of the emission spectra of an Er^{3+}-doped fiber ring laser with CO absorption in the cavity. The absorption cell contained 1 mbar of CO with a total pressure of 500 mbar. The referential transmission spectrum of CO calculated from HITRAN database (green) is superimposed with one of the spectra

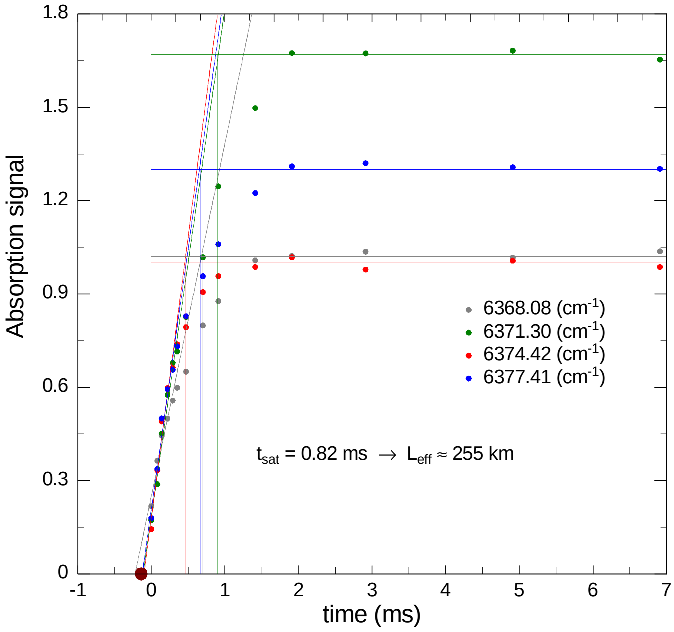

Figure 4.14 Development of the absorption signal as a function of time of four absorption lines evaluated from Fig. 4.13

In order to determine the sensitivity, four different absorption lines were evaluated according to (Eq. 2.8). By plotting the absorption signal over time one can determine the saturation time t_s. This is taken out of the intersection of the fit obtained from the linear increase slope with the horizontal line that corresponds to the signal at saturation. From the saturation time, the sensitivity of the laser can then be determined by the (Eq. 2.19) multiplied by the speed of light. The results are shown in Fig. 4.14. The sensitivity of the fiber ring laser to intracavity absorption is L_{eff} = 255 km by not taking the filling factor into account.

The effective absorption path length of the ring laser was enhanced by a factor of three compared to a linear configuration with the same length of the cavity [17]. It can be as well determined from Fig. 4.14 the sensitivity for each pulse. This is important for some measurements in which the sensitivity must be adjusted to a certain value such as the ones performed for breath measurements presented in the previous section.

Conclusion and Perspectives

A broadband Er^{3+}-doped fiber laser in the spectral range of 6220 cm^{-1} to 6540 cm^{-1} was developed for high sensitive absorption measurements in the laser resonator. A conventional laser diode at 980 nm was used as pump source. The emission wavelength can be tuned over the full range by moving an intracavity lens. The input mirror was directly placed onto the fiber end. The other fiber end was antireflective coated by vapor deposition.

Real time intracavity absorption spectra of CO_2 contained in exhaled human breath were recorded. The sensitivity of measurements with a pulsed laser applied in this experiment was set to 6 km by using a well defined pulsed laser operation. It does not depend on laser parameters and on broadband cavity losses. The effective absorption path length provided by this laser is 130 m by taking into account the filling factor of the cavity with the absorber.

A gas flow system was developed for calibration. It consists of two calibrated gas-flow controllers that allow to regulate the CO_2 and N_2 flows up to 1000 sccm. With this gas system the calibration was performed and confirmed by using theoretical data from the HITRAN database. Therefore this system enables accurate measurements of sample concentrations.

The CO_2 concentration in exhaled breath before and after smoking was investigated. The CO_2 concentration present in a single exhalation was experimentally demonstrated to be higher before smoking $n_{CO2} = 5.35$ % compared to after smoking $n_{CO2} = 5.02$ %.

The breath measurements were performed with an open absorption cell at atmospheric pressure for testing purposes. A gas filling system was planned and developed with a pressure controlled closed cell. With this system, accurate low-pressure measurements can be performed avoiding pressure line broadening.

This experiment performed with ICAS has proven to be a promising technique in the field of medical breath analysis. It is demonstrated to be reliable for time-resolved measurements of CO_2 concentration in exhaled breath. This opens a new gate for further experiments with other gases contained in human breath however in much lower concentrations, such as hydrogen cyanide (HCN), acetylene (C_2H_2), Carbon monoxide (CO), Ammonia (NH_3) or ethane (C_2H_6).

Sensitivity enhancement was achieved by employing a ring laser. The recording and evaluating of time-resolved intracavity absorption spectra of CO were demonstrated. The sensitivity of the fiber ring laser to intracavity absorption corresponds to $L_{eff} = 255$ km. The effective absorption path length of the ring laser was enhanced by a factor of three compared to a linear configuration with the same length of the cavity. Thus the detection of the molecules mentioned above in even lower concentrations can be achieved.

Bibliography

[1] Govind P. Agrawal, *Applications of Nonlinear Fiber Optics*, Academic Press, San Diego (2001)

[2] J. Limpert, T. Schreiber and A. Tünnermann, *Fiber Based High Power Laser Systems*

[3] S.K Turitsyn, J. D. Ania-Castanón, S. A. Babin, V. Karalekas, P. Harper, D. Churkin, S. I. Kablukov, A. E. El-Taher, E.V. Podivilov, and V. K. Mezentsev, *270-km Ultralong Raman Fiber Laser*, PRL 103, 133901 (2009)

[4] Hotan Shalibeik, *Rare-earth-doped fiber lasers and amplifiers*, Cuvillier, Göttingen (2007)

[5] John M. Senior, *Optical fiber communications: principles and practice,* Third Edition, Person Education Limited, UK (2009)

[6] Mário Ferreira, Óptica e Fotónica, Lidel (2003)

[7] Orazio Svelto, *Principles of Lasers,* Plenum Press, New York (1998)

[8] W. Koechner, *Solid State Laser Engineering*, Springer, USA (2006)

[9] Michel G. F. Digonnet, *Rare-Earth-Doped Fiber Lasers and Amplifiers,* Marcel Dekker, Standford, California (1993)

[10] Nick Usechak, *Mode-Locked Fiber Lasers and their Applications,* New York (2002)

[11] Andrew Weiner, *Ultrafast optics,* John Wiley & Sons, New Jersey (2009)

[12] Kristin M. Spaulding, Darryl H. Yong, Arnold D. Kim, and J. Nathan Kutz - *Nonlinear Dynamics of Mode Locking Optical Fiber Ring Lasers* - Vol. 19, No. 5/May 2002/J. Opt. Soc. Am. B

[13] E. Desurvire, Erbium-doped Fiber Amplifiers, Principles and Applications, John Wiley & Sons, New York (1994)

[14] P.C. Becker, N.A. Olsson, and J. R. Simpson - *Erbium Doped Fiber Amplifiers: Fundamentals and Technology*, Academic Press, San Diego (1999)

[15] W. Demtröder: *Laser Spectroscopy*, Springer Ser. Chem. Phys., Vol 5 (Springer Berlin, Heidelberg 1988)

[16] J. Michael Hollas, *Modern Spectroscopy*, 4th edition, Wiley (2004)

[17] B. Löhden, S. Kutnezova, K. Sengstock, V.M Baev, *Fiber laser intracavity absorption spectroscopy for in situ multicomponent gas analysis in the atmosphere and combustion environments*, Appl. Phys. B, DOI 10.1007/s00340-010-3995-9 (2010)

[18] J.u. White, J. Opt Soc. Am. 32, 285 (1942)

[19] H. Edner, P Ragnarson, Spannare, S. Svanberg, Appl. Opt. 32, 327 (1993)

[20] O’keefe, D.A.G Deacon, Rev. Sci. Instrum. 59, 2544 (1998)

[21] Romanini, K. K. Lehmann, J. Chem. Phys. 99, 6287 (1993)

[22] V.M. Baev, T. Latz, P.E. Toschek, *Laser Intracavity absorption spectroscopy,* Appl. Phys. B 69 171-202 (1999)

[23] J. Sierks, T. Latz, V.M. Baev, P.E. Toschek, *Proceedings of the 1996 European Quantum Electronics Conference (EQEC’96)*, 8-13, September 1996, Hamburg, p100, QWB6

[24] J. Hünkemeier, R. Böhm, V.M Baev, P.E. Toschek, *Spectral dynamics of multimode* Nd^{3+}*- and* Yb^{3+}*-doped fibre lasers with intracavity absorption*, Opt. Commun. 176 (2000) 417-428

[25] Mo Li, Kun Lio, Wencai Jing, and Gang-Ding Peng, *Fiber Ring Laser Intra-cavity Absorption Spectroscopy for Gas Sensing: Analysis and Experiment*, Opt. Soc. Vol 14, March 2010, pp 14-21

[26] J. Hernandez-Cordero, T.F. Morse, IEICE Trans. Electron. 83 (2000) 371.

[27] Y. Zhang, M. Zhang, W. Jin, H. Ho, M.S. Demokan, X.H. Fang, B. Culshaw, G. Stewart, Opt. Commun. 234, 435 (2004)

[28] G. Stewart, P. Shields and B. Culshaw, *Development of fibre laser system for ring-down and intracavity gas spectroscopy in the near-IR*, Meas. Sci. Technol. 15 (2004) 1621-1628

[29] R. Böhm, A. Stephani, V.M. Baev, P.E. Toschek: Opt. Lett. 18, 1955 (1993)

[30] S. Wu, A. Yariv, H. Blauvelt, N. Kwong, Appl. Phys. Lett. 59 1156 (1991)

[31] P. André, *Componentes Optoelectrónicos*, Tese de Doutoramento, Universidade de Aveiro, 1999

[32] Mário F.S. Ferreira, *Nonlinear effects in optical fibers*, John Wiley & Sons (2011)

[33] L.S. Rothman, I.E. Gordon, A. Barbe, D. ChrisBenner, P.F. Bernath, M. Birk, V. Boudon, L.R. Brown, A. Campargue, J.-P. Champion, K. Chance, L.H. Coudert, V. Dana, V.M. Devi, S. Fally, J.-M. Flaud, R.R. Gamache, A. Goldman, D. Jacquemart, I. Kleiner, N. Lacome, W.J. Lafferty, J.-Y. Mandin, S.T. Massie, S.N. Mikhailenko, C.E. Miller, N. Moazzen-Ahmadi, O.V. Naumenko, A.V. Nikitin, J. Orphal, V.I. Perevalov, A. Perrin, A. Predoi-Cross, C.P. Rinsland, M. Rotger, M. Šimecková, M.A.H. Smith, K. Sung, S.A. Tashkun, J. Tennyson, R.A. Toth, A.C. Vandaele, J. Vander Auwera, J. Quant. Spectrosc. Radiat. Transf. **110**, 533 (2009)

[34] T. H. Risby and S. F. Solga, *Current status of clinical breath analysis*, Appl. Phys. B 85, 421 (2006).

[35] W. Q. Cao and Y. X. Duan, *Breath analysis: Potential for Clinical Diagnosis and Exposure Assessment*, Clin. Chem. 52, 800 (2006).

[36] E. R. Crosson et al., *Stable Isotope Ratios Using Cavity Ring-Down Spectroscopy: Determination of* $^{13}C/^{12}C$ *for Carbon Dioxide in Human Breath*, Anal. Chem. 74, 2003 (2002).

[37] A. A. Kosterev, A. L. Malinovsky, F. K. Tittel, C. Gmachl, F. Capasso, D. L. Sivco, J. N. Baollargeon, A. L. Hutchinson, and A. Y. Cho, *Cavity ringdown spectroscopic detection of nitric oxide with a continuous-wave quantumcascade laser*, Appl. Opt. 40, 5522 (2001).

[38] S. Dill, J. J. Payne-James, J. J. Misiewicz, G. K. Grimble, K. McSwiggan, K. Pathak, A. J. Wood, C. M. Scrimgeour, and M. J. Rennie, *Evaluation of* $_{13}$*C-urea breath test in the detection of Heliobacter pylori and in monitoring the effect of tripotassium dicitratobismuthate in non-ulcer dyspepsia*, Gut. 31, 1237 (1990).

[39] F. Di Francesco, R. Fuoco, M. G. Trivella, and A. Ceccarini, *Breath analysis: trends in techniques and clinical applications*, Microchem. J. 79, 405 (2005).

[40] R. F. Machado et al., *Detection of Lung Cancer by Sensor Array Analyses of Exhaled Breath*, Am. J. Respir. Crit. Care Med. 171, 1286 (2005).

[41] W. L. Wood, D. J. Higbee, M. Gooldy, S. Glogowski, R. Fitzpatrick, R. J. Karalus, T. D. Wood, and D. J. Mangino, *Analysis of Volatile Metabolites by Gas Chromatography-Mass Spectrometry*, Spectroscopy 21, 20 (2006).

[42] R. Polikar, R. Shinar, V. Honavar, L. Udpa, and M. D. Porter, *Detection and Identification of Odorants Using an Electronic Nose*, in Proceedings of IEEE 26th International Conference Acoustics, Speech and Signal Processing 5, 3137 (2001).

[43] Mihalcea, R.M.; Baer, D.S.; Hanson, R.K. *Tunable diode-laser absorption measurements of NO2 near 670 and 395 nm*, *Appl. Opt.* 1996, *35*, 4059–4064.

[44] Baer, D.S. Hanson, R.K. Newfield, M.E. Gopaul, N.K.L.M. *Multiplexed diode-laser sensor system for simultaneous H2O, O2, and temperature measurements*, *Opt. Lett.* 1994, *19*, 1900–1902.

[45] T. Fritsch, P. Hering and M. Mürtz, *Infrared laser spectroscopy for online recording of exhaled carbon monoxide – a progress report*, J. Breath Res. 1 (2007) 014002 (8pp)

[46] Manfred Mürtz, *Breath Diagnostics Using Laser Spectroscopy*, Optics & Photonics News, January 2005